# FORMATION AND POSITIONING OF THE MAGNETOSOME CHAIN IN *MAGNETOSPIRILLUM MAGNETICUM* AMB-1

# FORMATION AND POSITIONING OF THE MAGNETOSOME CHAIN IN *MAGNETOSPIRILLUM MAGNETICUM* AMB-1

By

LUCAS LE NAGARD,
B.Sc.

A Thesis
Submitted to the School of Graduate Studies
in Partial Fulfillment of the Requirements
for the Degree
Master of Science

McMaster University

MASTER OF SCIENCE (2018) McMaster University
(Physics) Hamilton, Ontario

TITLE: Formation and positioning of the magnetosome chain in *Magnetospirillum magneticum* AMB-1

AUTHOR: Lucas Le Nagard,
B.Sc.(ESPCI Paris)

SUPERVISORS: Dr. Cécile Fradin & Dr. Adam Hitchcock

NUMBER OF PAGES: 1, 84

# Abstract

Magnetotactic bacteria are a group of prokaryotes that share the ability to align with external magnetic fields, due to the presence within their cytoplasm of one or several chains of nanometer-sized magnetic crystals called the magnetosomes. The orientation of the chain within the cell is critical for magnetotaxis, which allows these bacteria to swim along the geomagnetic field lines. To do so, the magnetic moment and thus the chain need to lie parallel to the swimming direction which, for elongated bacteria such as AMB-1, is roughly parallel to the long axis of the cell. In most studies, the alignment between the magnetic moment and the cell axis is taken for granted, however no precise measurement has been performed to confirm this. In this thesis, experiments performed to test this assumption are presented, and the results show that for most studied bacteria the alignment is not perfect. The effect on the orientation distributions is discussed and accounted for in the analysis performed to measure the magnetic moment of individual bacteria.

A second project presented in this thesis is focused on the biomineralization process in AMB-1. Magnetotactic bacteria synthesize crystals characterized by a well-controlled morphology and a high chemical purity, which makes them interesting for biomedical applications. To study how these crystals are produced, we used scanning transmission X-ray microscopy, and preliminary results show that this tool is suitable for studying this complex process. The methods developed and improved during this MSc to perform these experiments are presented, and the first results show an evolution in the spectroscopy of the magnetosomes as they grow.

# Preface

This thesis is organized as a sandwich thesis, in which the manuscripts of a paper and a conference paper written during this MSc are included. It starts with an introduction chapter that provides a general background on magnetotactic bacteria and the physical concepts needed to understand the two main projects presented here. In a second chapter, the methods used to perform the experiments and analyze their results are detailed. Chapter 3 presents the main findings of this MSc, through two manuscripts and two supplementary sections. Finally, the last chapter presents a general conclusion on the work presented in this thesis.

# Acknowledgements

This MSc at McMaster has been a formidable experience, during which I have had the immense pleasure to meet, work and hang out with many wonderful people. I will try to find words to thank them all here, as they really made these two years unforgettable. First and foremost, I would like to thank my supervisors Cécile and Adam for providing excellent guidance during this MSc. They both are amazing mentors and working with them for two years was fantastic. Adam, thank you for being so enthusiastic about everything you do, your excitement for science is contagious! Cécile, thank you for always finding the time to provide great advice, I will remember our long discussions trying to think of all the crazy possibilities for the orientation of a cell and its magnetic moment in a field. Dennis, I also want to thank you for everything you have taught me about these bacteria. None of the work presented in this thesis would have been possible without your continued support. Each of you, in your respective scientific areas, taught me that being passionate about what you do is the key for doing great research, and I will always remember that.

I would also like to thank everyone in the Hitchcock and Fradin groups, particularly Xiaohui, Lis and Michael. You made these two years really fun, and it was a pleasure to share good and bad fortune in the lab and at the STXM with you. Murtuza and Liu, thank you for your help on the misalignment project, it would have taken me much longer to finish this project without you. In Las Vegas, I also want to thank you Viviana for your help with the cultures and for welcoming me to the lab during my visit there. Finally, to my friends in the KDV lab: it has been great to hang out with you all, and it is always good to know that someone in the building can help out if you need a 3D printer or a nitrogen cylinder!

I would not have been able to do any STXM experiment without the valuable help of the people working on the STXM beamlines at Soleil, the CLS and the ALS, so thank you Sufal, Rachid, Jian, David and everyone maintaining the beamlines. Back to McMaster, I would like to thank Marcia for training me on the TEM. I'm also grateful to Cheryl, Rose, Hope, Tina and Mara at the physics office for always being there to help and making sure that everything in the department runs smoothly.

Many thanks also to the people from McMaster facility and cleaning services, without whom we would spend most of our time fixing and cleaning the labs instead of doing research.

In France, I would like to thank my parents and my brother for always believing in me. I owe you so much, thank you for always showing interest in what I do, it means a lot to me. Last but most certainly not least, I want to thank you Clémentine. There are no words to describe how important your support, kindness and humor are to me. You give me happiness in every moment spent with you and strength to pursue my dreams of an academic career. Both mean the world to me. Thank you for embarking me with you on this wonderful adventure to Canada, I am ready for the next one in Scotland!

# Contents

# List of Figures

# Chapter 1

# Introduction

The discovery of magnetotactic bacteria (MTB), which migrate along magnetic field lines, opened a new field of research that could lead to important applications in biomedical science and biorobotics. The directional motion of MTB is made possible by the presence of a chain of magnetic crystals within the cytoplasm, and relies on the fact that the resulting magnetic moment is generally aligned with the swimming direction. In this thesis, the formation and placement of the magnetosome chain within the cell are studied. In a first project, the magnetic moment of individual MTB is measured, and its orientation with respect to the cell axis is investigated. To do so, the motion of MTB placed in an external magnetic field is studied with optical microscopy. In a second project, the way MTB produce these crystals is studied with scanning transmission X-ray microscopy (STXM), an X-ray imaging technique that combines spectroscopy and microscopy. This introductory chapter thus starts with a review of the current knowledge on MTB, continues with a presentation of the background required to understand how a single MTB interacts with a magnetic field, and finally introduces the basic principles of X-ray absorption spectroscopy.

## 1.1 Magnetotactic bacteria: a diverse group of microorganisms

### 1.1.1 Discovery of magnetotactic bacteria

The first observation of magnetotactic bacteria was reported in 1963 by Salvatore Bellini, in a short manuscript that remained unnoticed for many years until 2009 [1,2]. In his study, Bellini described the intriguing swimming behaviour displayed by microorganisms of various morphologies in different environmental freshwater samples. He observed that these bacteria swam persistently northward when placed into a hanging drop of water and understood that their direction of motion was governed by the geomagnetic field. He concluded that these bacteria had to possess some sort of internal magnetic compass that made them align with externally applied magnetic fields and proposed the name "magnetosensitive bacteria" to designate bacteria exhibiting this particular behaviour. Unfortunately, Bellini could not get the permission from his university to publish his discovery in a peer-reviewed scientific journal.

In 1975, Blakemore independently re-discovered in Massachusetts bacteria that migrated persistently northward [3]. He named this behaviour "magnetotaxis" and referred to bacteria exhibiting such behaviour as "magnetotactic bacteria" (MTB). Electron microscopy observations showed that the ability to perform magnetotaxis originates from the presence of a variable number of magnetic crystals within the cytoplasm of MTB. Such crystals confer to the cell a permanent magnetic dipole moment, causing it to align with external magnetic fields. Magnetotaxis thus refers to the passive alignment of the cells with external magnetic fields combined with an active swimming motion along the field lines.

The fact that MTB migrate along the magnetic field lines makes them easy to detect in environmental samples. In addition, early studies reported that MTB are present in many, if not all, regions of the world [4]. However, isolating MTB and growing them in axenic (*i.e.* containing only one species) culture has proven to be challenging. The first isolation of MTB in pure culture was reported in 1979 [5]. Strain *Magnetospirillum magnetotacticum* MS-1, originally named *Aquaspirillum magnetotacticum* by

Blakemore, was isolated from freshwater mud and successfully grown in a chemically defined growth medium. Isolation in pure culture is a key step in bacterial research and is usually required to study the properties of a specific strain. Mössbauer spectra recorded on MS-1 after its isolation in pure culture showed that the magnetic crystals synthesized by this strain are made of magnetite ($Fe_3O_4$) [6]. Other MTB present in the environmental sample from which MS-1 was isolated could not be grown at that time, illustrating the difficulty of culturing MTB.

### 1.1.2 Ecology and phylogenetic diversity

MTB are a group of prokaryotes ubiquitous in aquatic habitats. They have been observed on all continents and are naturally present in sediments of diverse environments, ranging from freshwater habitats to marine and even hypersaline environments [7]. Most MTB species are obligately microaerophile, which means that they need a small amount of dissolved $O_2$ made available to them for growth. Microaerophile organisms need $O_2$ because they are not capable of anaerobic respiration, but are at the same time poisoned by high $O_2$ concentrations. The particular $O_2$ requirements of MTB explain why these bacteria are predominantly found at the transition zone between oxic ($O_2$ - rich) and anoxic ($O_2$ - deprived) conditions or slightly below this oxic-anoxic interface (OAI) [8]. Sediments or water columns that display a well-defined OAI are more likely to contain MTB and are characterized by the presence of two opposing gradients: one of dissolved $O_2$ decreasing downward from the surface, and one of reduced compounds (principally sulfur species) decreasing upward from deeper regions. MTB are therefore a typical example of gradient-sensitive organisms and this property needs to be taken into account when developing methods to culture these bacteria. It is also probably the reason why MTB developed magnetoaxis, which allows them to efficiently swim up and down gradients along the geomagnetic field lines.

Most MTB have been observed in habitats with pH values near neutral and are mesophile, which means that they grow best at ambient temperature. However, Lefèvre and coworkers [9] recently reported the presence of MTB in water and sediments sampled at the Great Boiling Springs (Nevada, USA). These springs range

from ambient temperature to almost 100 °C and MTB were found at temperatures ranging from 30 to 62 °C, making them the first moderately thermophilic MTB ever observed. Additionaly, Lefèvre also reported the discovery and isolation of obligately alkilophilic MTB in highly alkaline (pH > 9.0) muds [10]. These bacteria did not grow at pH lower than 8.0, proving their need for alkaline conditions. These findings show that extremophilic MTB do exist, and that the currently known diversity of MTB is still likely underestimated [7].

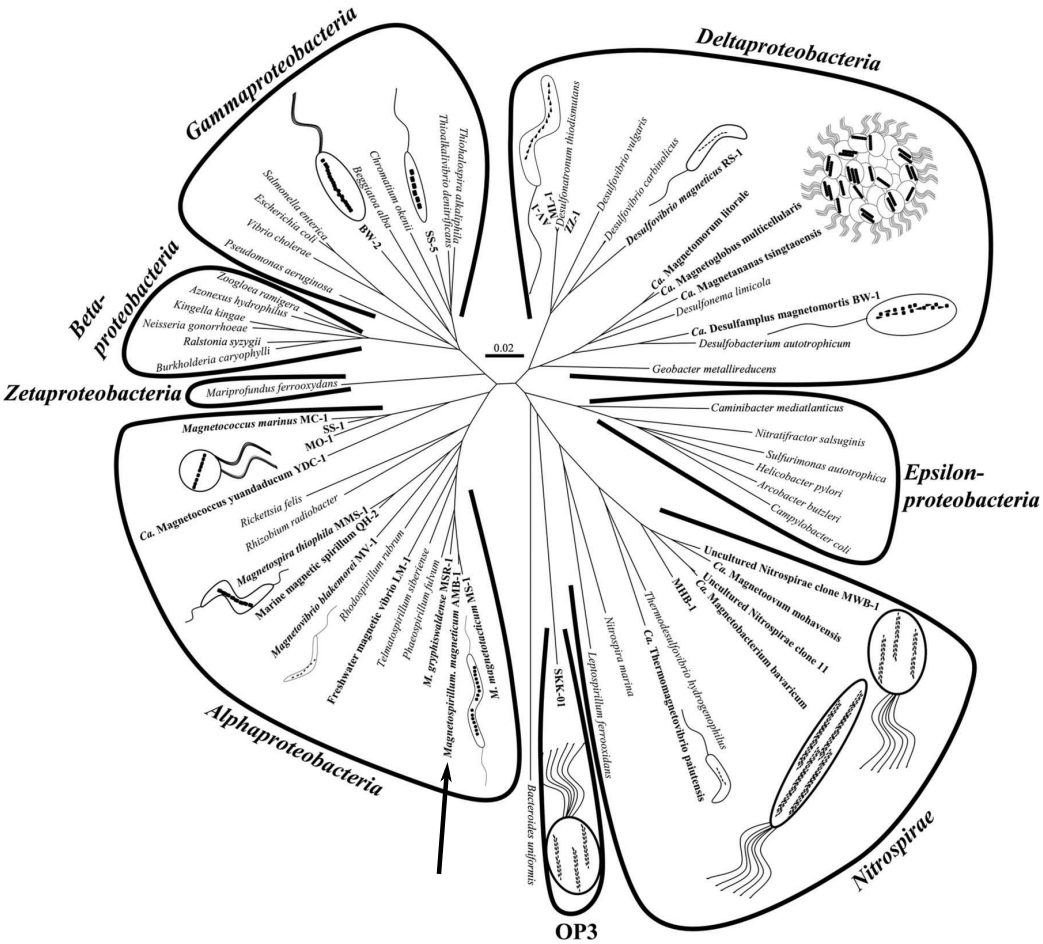


Figure 1.1: Phylogenetic distribution of both cultured and uncultured MTB in the *Proteobacteria* phylum, the *Nitrospirae* phylum and the candidate division OP3. MTB are in bold. The arrow indicates strain AMB-1, used in the work presented in this thesis. Reproduced from [7] with permission from the *American Society for Microbiology (ASM)*.

Living organisms are usually classified into three main domains: *Bacteria*, *Archaea* or *Eukaryota*. All magnetotactic prokaryotes studied so far belong to the domain *Bacteria*, no organism responding to magnetic fields in a similar way as MTB having been found in the other two domains yet. However, the term magnetotactic bacteria still refers to a phylogenetically diverse group. Fig. 1.1 presents only a small portion of the phylogenetic diversity of cultured and uncultured MTB within the domain *Bacteria*. MTB are associated with five lineages within this domain: the *Alphaproteobacteria*, *Gammaproteobacteria* and *Deltaproteobacteria* classes (all within the *Proteobacteria* phylum), the *Nitrospirae* phylum and the candidate division OP3. Most known MTB and almost all cultured strains belong to the *Proteobacteria* phylum [7]. Division into different phyla or classes is the result of differences at the genetic and molecular levels, and often translates into different phenotypes or physiological requirements. Conducting a phylogenetic analysis on MTB from an unknown, uncultured species can therefore lead to a better understanding of this strains's specific requirements and help devise an appropriate growth medium to culture it.

### 1.1.3 Structural properties - Cell morphology and magnetosomes

#### Cellular morphology

As expected for a phylogenetically diverse group, MTB display a great variety of cellular morphologies. However, MTB of different species still share some common morphological characteristics. All known MTB possess at least one flagellum and are motile. They are Gram-negative, *i.e.* are characterized by a specific cell envelope made of two membranes (the outer membrane and the plasmic membrane, which differ in composition) and a thin peptidoglycan layer in between (Fig. 1.2). In the Gram staining test, the crystal violet dye binds to peptidoglycan. For Gram-negative bacteria, the peptidoglycan layer is thin enough that the CV dye is washed away by quick exposure to alcohol, causing the cell to lose its purple color, thus returning a negative staining result.

The simplest way to classify microorganisms is to define groups based on cell morphol-

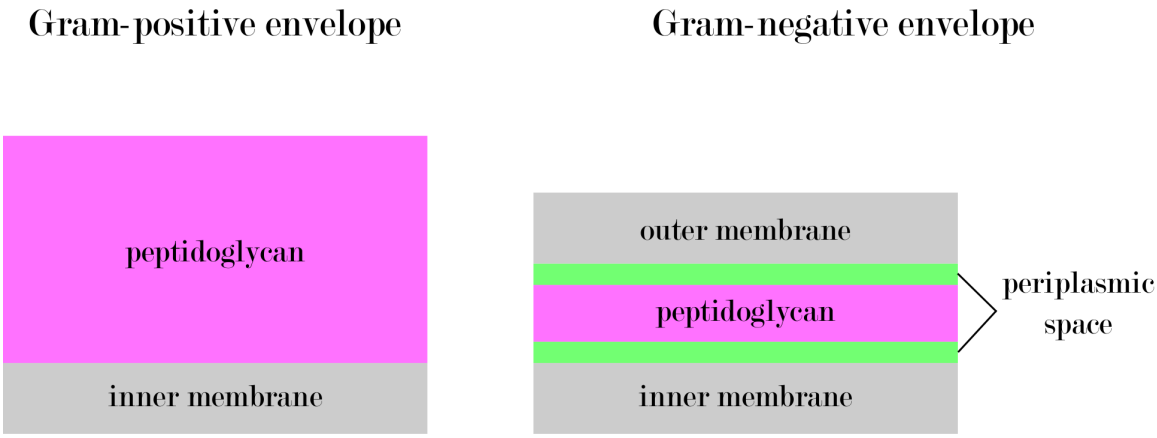


Figure 1.2: Schematic description of Gram-positive and Gram-negative cell envelopes.

ogy. For instance, bacteria that are spherical or generally round belong to the group coccus. Helical bacteria are referred to as spirilla, rod-shaped bacteria of various sizes are called bacilli and bacteria that exhibit a curved-rod shape are called vibrios. MTB belonging to these four common groups have been found in the environment, however magnetotactic cocci (magnetococci) appear to be among the most abundant, especially in freshwater habitats [11]. To date, however, only three magnetococci strains have been axenically cultured: MC-1, MO-1 and IT-1 [12]. The first MTB strain to be isolated in pure culture, MS-1, is a spirillum of about 4-6 $\mu$m in length and 0.25 $\mu$m in body width [5]. Other freshwater spirilla such as AMB-1 [13] and MSR-1 [14] have later been isolated and grown in pure culture. Perhaps the most unusual morphotype exhibited by some MTB is that of the so-called multicellular magnetotactic prokaryotes (MMP). These organisms are made of a variable number of Gram-negative cells (usually 10 to 60) that form a motile, roughly spherical aggregate of 3 to 12 $\mu$m in diameter [7]. Interestingly, individual cells that detach from the aggregate cannot survive and die quickly.

All known MTB are motile by means of flagella, however different strains of MTB can be characterized by different flagellar arrangements. For instance, magnetospirilla AMB-1, MSR-1 and MS-1 possess two polar flagella, one at each end of their body [13, 14]. Other MTB, such as the marine vibrio strain MV-1 [7] or the freshwater strain RS-1 [15] possess only one polar flagellum. The marine coccus MC-1 is

bilophotrichous, meaning that it exhibits two bundles of flagella on one side of the cell [16]. Finally, MMP display a complex flagellar apparatus, with flagella covering the whole organism (approximately 30 flagella per cell constituting the aggregate, only on the environment-facing part of each cell) [17].

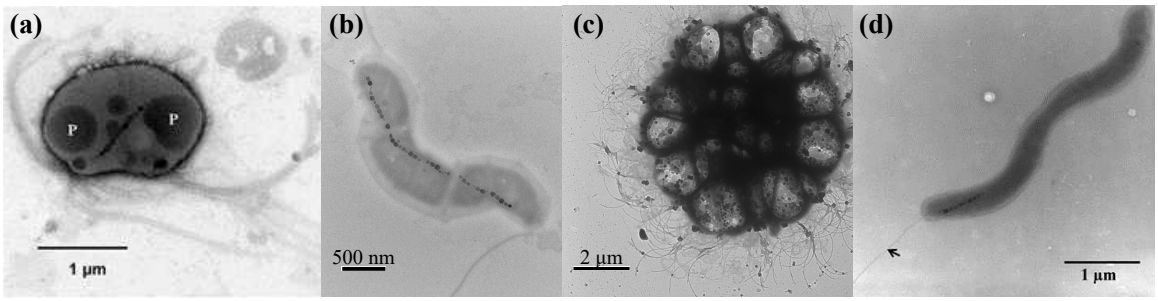


Figure 1.3: Electron microscopy images of four different MTB strains illustrating the diversity of MTB morphotypes. **(a)** Bilophotrichous coccus (MC-1 strain). Reproduced from [16] with permission from *Microbiology Society*. **(b)** Magnetospirillum AMB-1, with one polar flagellum at each end of the cell. **(c)** Multicellular magnetotactic prokaryote (MMP). Flagella can be seen all around the organism's body. **(d)** Dividing cell of magnetovibrio strain MV-1. Reproduced from [18] with permission from *Microbiology Society*.

### Magnetosomes

A common feature of MTB is the presence, within the cytoplasm, of specific organelles called magnetosomes, each made of a single magnetic crystal surrounded by a lipid membrane. The size, the chemistry and the crystallography of these crystals vary from one species to the other, but each strain is able to control these parameters and usually produces only one type of magnetosomes [11].

The chemical composition of magnetosomes is relatively simple: MTB produce relatively high purity crystals made either of magnetite ($Fe_3O_4$) or greigite ($Fe_3S_4$). At least one MTB is capable of producing both minerals [19]. However, a great diversity of crystal morphologies is observed within cultured and uncultured MTB strains. The shape of the crystals, which can be studied by high-resolution transmission electron

microscopy (TEM), can indeed vary from cuboctahedral structures to elongated prismatic morphologies and even bullet-shaped crystals (Fig. 1.4).

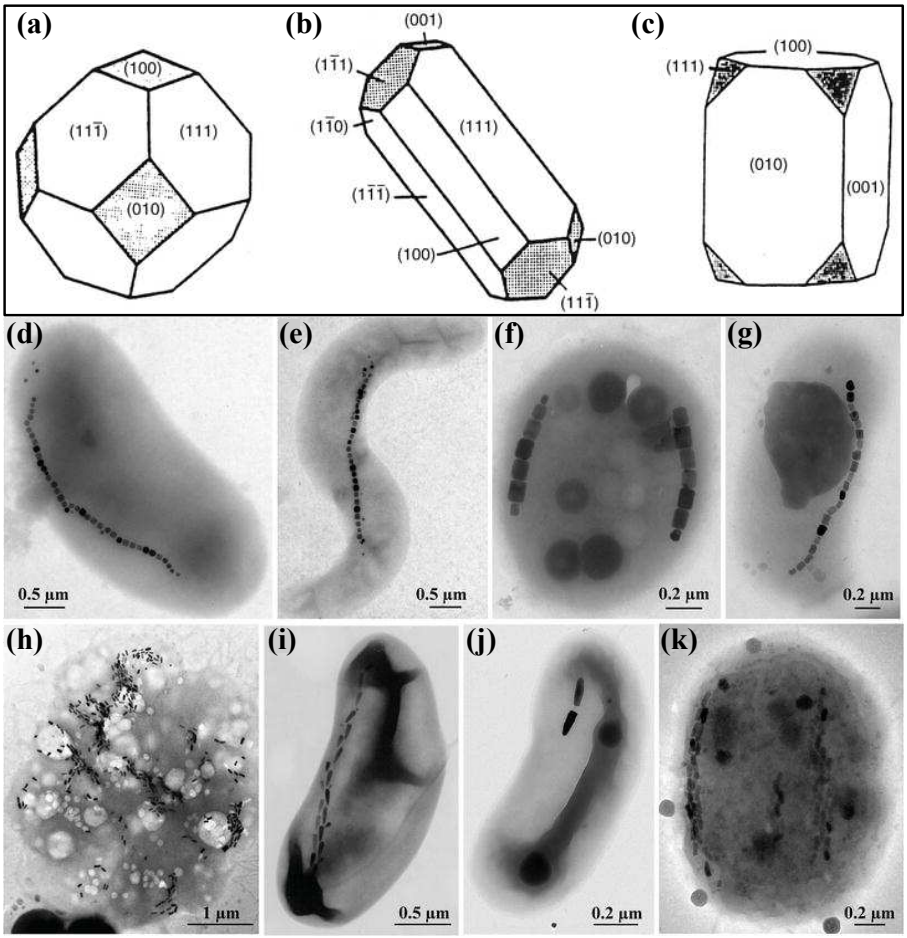


Figure 1.4: Diversity of magnetosome morphologies. **(a)-(c)** Examples of common, TEM-derived, idealized, crystallographic structures observed for magnetosomes of various species. **(a)** Cuboctahedral morphology, observed for both magnetite and greigite magnetosomes. **(b)** & **(c)** Example of magnetite (b) and greigite (c) elongated prismatic morphologies. **(d)-(k)** Brightfield TEM images of intact MTB cells of various species containing various types of magnetosomes.**(d)** & **(e)** Cuboctahedral crystals. **(f)** & **(g)** Elongated-prismatic crystals. **(h)-(k)** Anisotropic, bullet-shaped crystals. Figure adapted from [8] with permission from *Springer*.

The fact that MTB precisely control the size of their magnetosomes has a direct impact on the magnetic properties of these particles. Depending on their size, particles

made of magnetite or greigite can be superparamagnetic, single-domain or multi-domain. Most MTB synthesize magnetosomes that range from 35 to 140 nanometers in size, which places them in the single-domain (SD) state [11]. SD particles are uniformly magnetized, and their direction of magnetization remains constant over time in the absence of a strong external magnetic field. For a smaller particle, thermal fluctuations are no longer negligible. Thermal fluctuations affect the orientation of individual spins within the particle, and cause the magnetization of the particle to change randomly. Energy barriers are associated with such reorientations, and are proportional to the number of atoms, *i.e.* to the volume of the particle. Small, superparamagnetic particles therefore have low energy barriers and their time-averaged magnetization is equal to zero at room temperature in the absence of an external magnetic field (Fig. 1.5). On the other hand, in the case of large particles, the energy cost originating from the demagnetizing field (the field created by the particle itself) becomes so large that the particle adopts a multi-domain (MD) configuration, usually with some sort of closed-loop geometry. In that case the demagnetizing field and the associated energy are reduced, but the magnetic moment of the particle is also drastically decreased.

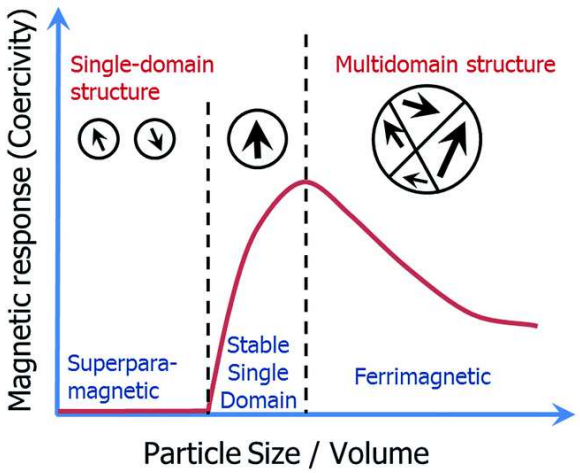


Figure 1.5: Schematic relationship between the magnetic response of individual particles made of magnetite and the particle size. The higher the coercivity, the more difficult (in terms of applied magnetic field) it is to change the magnetization of the particle. Figure reproduced from [20].

By controlling the size of their magnetosomes, MTB maximize the magnetic moment of each particle. However, the total magnetic moment of the cells would still be zero if the magnetosomes were randomly oriented in the cytoplasm. One can observe in Fig. 1.4 (d)-(k) that magnetosomes are assembled into one or several chains in MTB. In that case, the magnetic moment of each particle is likely to be more or less aligned with the axis of the chain, thus confering a significant total magnetic moment to the cell along its swimming direction. The organization into chains is made possible by the interplay between several proteins. In the case of strains AMB-1 and MSR-1, MamK and MamJ play a major role in maintaining the chain organization [21]. MamK is an actin-like protein that forms a rigid filament roughly aligned with the long axis of the cell, and MamJ is a protein that attaches magnetosomes to the MamK filament (Fig. 1.6). MamK has been found in many MTB, whereas MamJ has only been observed in *Magnetospirillum* [21].

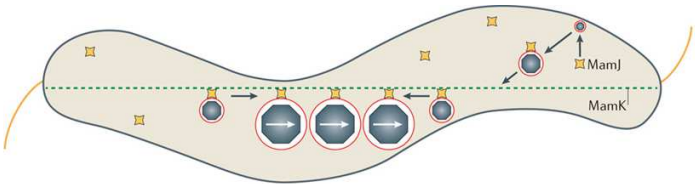


Figure 1.6: Schematic representation of the magnetosome chain in *Magnetospirillum*. Magnetosome alignement is due to the interplay between MamJ and MamK. In strain MSR-1, the chain is positioned at mid-cell. White arrows represent the orientation of the magnetic moment of each crystal. Reproduced from [21] with permission from *Springer*.

The biomineralization process has been thoroughly studied in MTB, principally in *Magnetospirillum*. Genetic studies on MTB have shown that a set of at least 30 genes are specifically involved in the biomineralization process [21]. Interestingly, these genes are clustered into a single chromosomal region, called the genomic magnetosomes island (MAI). Komeili and coworkers studied MTB strain AMB-1 and showed that the magnetosome membrane is an invagination of the cell membrane [22]. They also demonstrated the role of MamK by showing that the magnetosomes could no longer assemble in a chain when MamK was deleted. The role of MamJ was demonstrated by Scheffel and coworkers in MSR-1 [23]. Without this protein, magnetosomes

could not attach to the MamK filament and instead formed an aggregate favored by magnetic interactions. Based on these discoveries, a model has been proposed for biomineralization, chain formation and cell division in MSR-1 (Fig. 1.7). Many other proteins have been identified in the MAI, and their role is under continuous investigation. For instance, it has been shown that Mms5, Mms6 and MamD interact with magnetite and are likely to play a role in controlling the crystal growth [21]. It is also believed that MamB and MamM are involved in the transport of iron from the cytoplasm to the magnetosome membrane [21]. However, many details of the biomineralization mechanism are still poorly understood. It is for example still not clear how much and in which form iron accumulates in the cytoplasm, and how proteins are recruited to the magnetosome membrane.

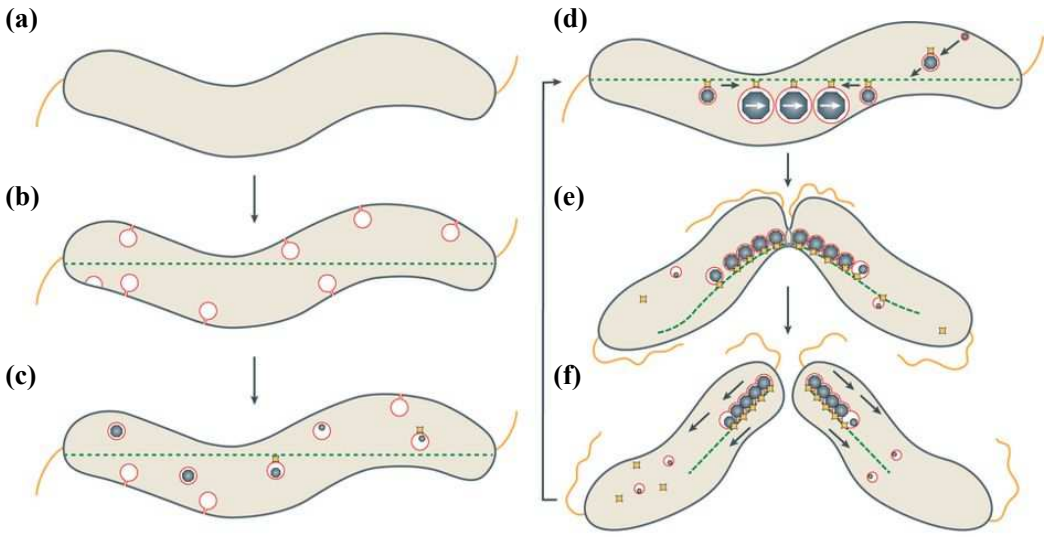


Figure 1.7: Biomineralization model for MSR-1. Starting from an hypothetical cell completely free of magnetosome in **(a)**, magnetosome vesicles are formed as invaginations of the cell membrane in **(b)**. **(c)** Magnetite biomineralization is initiated in the newly formed vesicles, which progressively attach to the MamK filament through the MamK-MamJ interaction. **(d)** Mature magnetosomes form a chain positioned at mid-cell that exhibits a permanent magnetic moment. **(e)** Cell division is initiated, two new flagella appear at mid-cell before separation of the two daugther cells. **(f)** Two daughter cells are obtained, each possessing roughly half of the magnetosomes of the mother cell. Chain moves to mid-cell and new magnetosomes are synthesized. Reproduced from [21] with permission from *Springer*.

### 1.1.4 The magneto-aerotaxis model

As a consequence of possessing a magnetosome chain, MTB passively align in external magnetic fields and actively swim along the magnetic field lines. Blakemore first proposed the term magnetotaxis [3] to describe the swimming strategy of MTB. In this model, MTB align with the geomagnetic field and are thought to have a preferred swimming polarity with respect to the field: they would preferentially migrate northward (North-seeking, NS) or southward (South-seeking, SS). One should note that NS bacteria swim towards the south pole of a magnet, while SS bacteria swim towards the magnetic north pole. Due to the inclination of the geomagnetic field lines, NS bacteria in the Northern hemisphere and SS bacteria in the Southern hemisphere migrate downward towards sediments and lower $O_2$ concentrations (Fig.1.8 (a)). According to the magnetotaxis model, MTB thus swim downward towards sediments and favorable growth condition, stop swimming when they reach this optimal region and start swimming again if a disturbance of the sediments displaces the cells to $O_2$ - rich regions [24]. As expected, MTB originally sampled in the Northern hemisphere were found to be North-seeking.

However, this simple model does not explain certain behaviours that have been observed later for MTB. For example, some MTB such as MC-1 are known to be obligately microaerophilic and would be driven to unfavorable anaerobic regions by a strictly polar magnetotaxis. Additionaly, MC-1 forms microaerophilic bands when grown in an $O_2$ gradient, while according to the simple magnetotaxis model they should migrate towards the bottom of the tube in which they are cultured. Discovery of such bacteria led to a modification of the magnetotaxis model, which was improved to take the aerotactic response of MTB into account in the magneto-aerotaxis model (Fig.1.8 (b)).

Two types of mechanisms have been identified: polar and axial magneto-aerotaxis. Axial magneto-aerotaxis, which is used by *Magnetospirillum* strains, is based on a temporal sensory mechanism similar to classical chemotaxis. MTB that exhibit axial magneto-aerotaxis are able to detect the instantaneous variations of $O_2$ concentration and to change their direction of motion accordingly: swimming along the magnetic

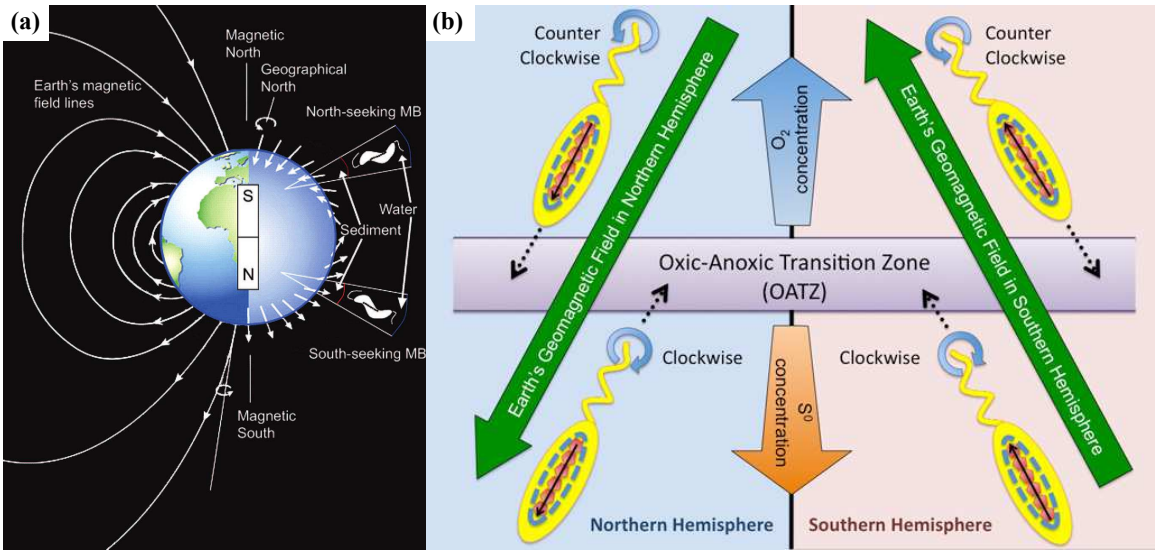


Figure 1.8: Magneto-aerotaxis enables MTB to efficiently find the oxic-anoxic interface. **(a)** Illustration of the inclination of the geomagnetic field lines. MTB in the Northern hemisphere are North-seeking under oxic conditions, while MTB in the Southern hemisphere are South-seeking. Reproduced with permission from [11]. Copyright (2008) *American Chemical Society*. **(b)** Illustration of the magneto-aerotaxis model. Cells swim along the magnetic field lines, in a direction imposed by the $O_2$ concentration. Reproduced from [25].

field lines, they have a higher probability of reversing their direction of motion if they swim away from ideal $O_2$ conditions, and a lower probability of doing so if they are swimming towards ideal conditions [24]. As a consequence, they perform longer runs towards ideal conditions, and shorter runs in the opposite direction.

On the other hand, polar MTB placed in oxic conditions swim northward (or to the south pole of a magnet) in the Northern hemisphere, and southward (or to a magnetic north pole) in the Southern hemisphere (state 1). In nature, this allows them to move towards deeper regions, where the $O_2$ concentration is reduced. They keep swimming in the same direction until the $O_2$ concentration goes below a certain threshold. At that point, they reverse their direction of motion and swim upward (state 2) until the $O_2$ concentration becomes larger than a second threshold. When they reach this second threshold, they go back to state 1.

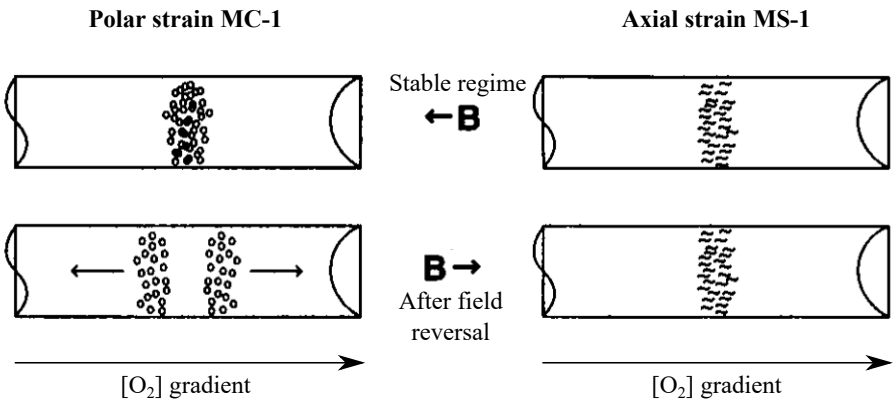


Figure 1.9: Polar vs axial magneto-aerotaxis. A microaerophilic band of polar strain MC-1 in an $O_2$ gradient is divided into two groups swimming in opposite directions when the magnetic field is reversed (left). A similar band of axial strain MS-1 is not affected (right). Adapted from [26] with permission from *Elsevier*.

Thus the major difference between polar and axial magneto-aerotaxis is that the axial mechanism is continuous while polar magneto-aerotaxis is best described by a two state model [24, 26]. In a microaerophilic band of polar MTB, when a constant field is applied, approximately half of the population swims in each direction in the stable regime. If the field is suddenly reversed, MTB align in the new field (cells passively rotate) but remain in the same swimming state (same direction of motion with respect to the field direction). Cells that were swimming downward (state 1) will therefore start swimming upward and will keep swimming in this direction since they will never encounter the low $O_2$ concentration threshold. Cells that were in state 2 will move in the opposite direction, never reaching the high $O_2$ concentration threshold. This leads to a separation of the microaerophilic band into two groups of cells swimming in opposite directions (Fig. 1.9 left). The band is recovered if the field is reversed again. In the case of axial MTB, a magnetic field reversal forces the cells to rotate but the microaerophilic band is not disturbed (Fig. 1.9 right) since axial MTB do not need a concentration threshold to reverse their direction of motion.

In both cases, magneto-aerotaxis makes the search of optimal conditions (usually the OAI) more efficient by reducing a three dimensional search problem to a one dimensional problem along the magnetic field lines. However, some questions remain

unanswered, such as the presence of some principally South-seeking MTB in the Northern hemisphere, or the presence of MTB at the equator, where the geomagnetic field lines are horizontal [7]. Additionally, it appears that the magnetotactic response of MTB can be affected by culturing conditions in the laboratory [7].

### 1.1.5 Applications of magnetotactic bacteria and magnetosomes

This section presents briefly two examples of potential applications for MTB and magnetosomes. The review from Yan and coworkers [27] presents many other applications.

The magnetic properties of MTB allow for an external control of their motion with externally applied magnetic fields, making them interesting for nanorobotics applications. A proof of concept of MTB's potential to perform simple tasks was provided by Martel and coworkers [28]. In their study, they showed that MTB could push micrometric beads in a direction controlled by the experimentalist. The beads were made of melamine-formaldehyde, and bacteria simply attached to the sticky surface of the beads. The authors reported an average speed of 7.5 $\mu m.s^{-1}$ for beads being pushed by a single bacterium, and said that the direction of motion could be tuned by changing the magnetic field direction. However, they did not provide data on how well they could control the direction of motion.

The most promising applications of MTB might actually be magnetosome-based applications. The high chemical purity of the magnetosome crystals and the presence of a biological membrane surrounding the crystal are in fact two properties that make these particles suitable for many biomedical applications. For example, Matsunaga and coworkers showed that magnetosomes could be used to detect and remove *Escherichia coli* bacteria in solution [29]. To do so, they first extracted magnetosomes from MTB, and then immobilized fluorescent anti *E. coli* antibodies on the magnetosomes. This step was made easier by the presence of the membrane surrounding the crystal, since membrane chemical modification is a known method in biochemistry. In the presence of *E. coli* cells, the magnetosomes attach to *E. coli*, forming bacteria-

magnetosomes aggregates that sediment much faster than unbound magnetosomes remaining free in solution. By comparing the fluorescence in solution before and after the aggregation process, they were able to build a calibration curve that would allow for the determination of the *E. coli* concentration in solution. Additionally, this method allows for the selective removal of *E. coli* bacteria from bacterial suspensions by magnetic extraction of the *E. coli* - magnetosomes aggregates.

### 1.1.6 *Magnetospirillum magneticum* AMB-1

Most of the work presented in the Results section of this thesis has been done on strain AMB-1, therefore it is useful to present this strain in more details here. *Magnetospirillum magneticum* was first observed and isolated in pure culture by Matsunaga and coworkers from freshwater sediments [13] and has become one of the most studied MTB strain. It is for example one of the few MTB for which the complete genome sequence is known [30]. The water sample from which this strain was isolated is characterized by an almost neutral, slightly acidic pH (between 6.5 and 7.0). This strain is helical in morphology, with an average cell length of about 3 $\mu$m [31,32] and a cell diameter of 0.4 to 0.6 $\mu$m [13]. AMB-1 produces cuboctahedral magnetosomes made of magnetite, with an average size per crystal of 50 nanometers [13]. These crystals are assembled in a chain within the cytoplasm, often discontinuous and fragmented into 2 to 5 subchains [33], as illustrated in Fig. 1.3 (b). Seong and Park reported an average swimming speed of 49 micrometers per second, independent of cell length [31].

Matsunaga and coworkers showed that AMB-1 is a facultative anaerobic (*i.e.* can survive in the absence of $O_2$), microaerophilic bacterium [13]. Interestingly, it was shown in some studies that AMB-1 also grows under aerobic conditions with drastically reduced magnetosome production [33,34], while Heyen and Schüler reported no growth for AMB-1 under these conditions [35]. AMB-1 possess two polar flagella and is characterized by an axial magneto-aerotaxis, using external magnetic fields as an axis but not as a direction [26]. As many other MTB, this strain forms microaerophilic bands when placed in an $O_2$ gradient.

## 1.2 Motion of MTB in external magnetic fields

### 1.2.1 Life at low Reynolds number

MTB, like many other bacteria, propel themselves by rotating their flagella. This section presents the main physical concepts associated with self-propulsion at low Reynolds number, which is the relevant regime for bacteria [36]. The way the propelling force is generated is a complex problem and is not discussed here. More details can be found in the review by Lauga [37], on which this section is based. The local flow field $\mathbf{u}$ of an incompressible Newtonian fluid is governed by the Navier-Stokes equations:

$$\rho\left(\frac{\partial}{\partial t}+\mathbf{u}\cdot\nabla\right)\mathbf{u}=-\nabla p+\eta\nabla^2\mathbf{u}, \tag{1.1}$$

$$\nabla\cdot\mathbf{u}=0, \tag{1.2}$$

where $\rho$ is the density of the fluid, $p$ is the pressure in the surrounding fluid and $\eta$ is the viscosity of the fluid. The stress tensor $\boldsymbol{\sigma}$ can be computed if the pressure and the flow field are known and is given by:

$$\boldsymbol{\sigma}=-p\mathbf{I}+\eta\left(\nabla\mathbf{u}+\nabla\mathbf{u}^T\right), \tag{1.3}$$

where $\mathbf{I}$ is the identity matrix. The force and the torque applied by the fluid on a body such as a bacteria are obtained by integrating $\boldsymbol{\sigma}$ along the body surface. However, the general Navier-Stokes equations are difficult to solve and some approximations are needed to make them easier to work with. For bacteria, a major simplification comes from the fact that their swimming motion is characterized by a low Reynolds number ($Re$). The Reynolds number is a dimensionless quantity that can be regarded as the ratio of the inertial and viscous terms in the Navier-Stokes equation describing a steady flow of typical velocity $U$ around a body of typical size $L$. In that situation, the inertial term $\rho\left(\mathbf{u}\cdot\nabla\right)\mathbf{u}$ and the viscous term $\eta\nabla^2\mathbf{u}$ can be rewritten as:

$$\rho\left(\mathbf{u}\cdot\nabla\right)\mathbf{u} \sim \frac{\rho U^2}{L}, \tag{1.4}$$

$$\eta\nabla^2\mathbf{u} \sim \frac{\eta U}{L^2}. \tag{1.5}$$

The Reynolds number is thus defined by:

$$Re = \frac{\rho L U}{\eta} \tag{1.6}$$

For an AMB-1 cell of length 3 $\mu$m swimming at an average speed of 50 $\mu$m.s$^{-1}$ in water ($\eta \sim 10^{-3}$ Pa.s, $\rho \sim 10^3$ kg.m$^{-3}$), a Reynolds number $Re \sim 10^{-4}$ is obtained. As a consquence, the inertial terms can be neglected and Eq. 1.1 can be rewritten to obtain a simplified Stokes equation:

$$\nabla p = \eta\nabla^2\mathbf{u}. \tag{1.7}$$

Consider a body, such as a bacteria, that suddenly stops swimming. The drag force applied to the body scales with $\sigma$ as $f_{drag} \sim \sigma L^2$. Since the bacteria moves at low $Re$, the drag force is dominated by the viscous drag and can thus be written as $f_{drag} \sim \eta U L$. Newton's second law gives:

$$\rho_B L^3 a \sim \eta U L, \tag{1.8}$$

where $\rho_B$ is the density of the bacteria, approximately equal to the density of water. The acceleration can be rewritten as $a \sim U^2/d$, where $d$ is the distance traveled by the bacteria before coming to a stop. Using Eq. 1.8, $d$ is written as:

$$d \sim \frac{\rho_B L^2 U}{\eta}, \tag{1.9}$$

which gives $d \sim 0.5$ nm. This means that the bacteria stops instantaneously in the absence of a propelling force. In contrast, organisms that swim at high $Re$ (*i.e.* humans) experience a drag force dominated by inertia, and coast for longer distances before coming to a stop. At low $Re$, the response of the surrounding fluid is thus instantaneous, which means that Newton's second law for forces ($\mathbf{F}_i$) and torques ($\mathbf{L}_i$) just becomes an instantaneous balance between fluid and external contribution:

$$\mathbf{F}_{ext}(t) + \mathbf{F}_{fluid}(t) = 0, \tag{1.10}$$

$$\mathbf{L}_{ext}(t) + \mathbf{L}_{fluid}(t) = 0, \tag{1.11}$$

### 1.2.2 Interaction with a magnetic field - Boltzmann statistics

This section presents the concepts of statistical physics used to analyze the behaviour of a magnetic moment placed in an external field and subject to thermal fluctuations. It is by comparing the experimental results to the model presented in this section that the existence of a misalignment between the cell axis and the magnetic moment was identified during this MSc.

As explained in 1.1.3, MTB possess one or several chains of single-domain (SD) magnetosomes. Jacobs and Bean considered the problem of a chain made of several SD spherical particles, and showed that the most stable configuration for the free arrangement of three SD particles is a chain with each particle's magnetization aligned with the chain axis [38]. For the free arrangement of four particles, a closed-loop configuration is more stable. However, if a particle is added to a pre-existing rigid chain of three or more particles, then its magnetization will be aligned with the chain axis. This model is appropriate for describing the magnetosome chain, since the SD particles are held in place by the rigid MamK filament.

The magnetosome chain can thus be seen as a rigid rod carrying a permanent magnetic moment $\boldsymbol{\sigma}$. At low applied magnetic fields, the effect of the magnetic susceptibility can be neglected and the magnetic moment can be considered constant. In this simple model, the magnetosome chain behaves like a single spin in an external magnetic

field, which corresponds to Langevin model for paramagnetism [39]. The orientation distribution of the magnetic moment with respect to the magnetic field is thus the result of the competition between thermal fluctuations and the magnetic interaction. The energy of magnetic interaction [40] is given by:

$$E_m(\theta, \phi) = -\mu B \cos\theta, \tag{1.12}$$

where $\theta$ is the angle between the field $\mathbf{B}$ and the magnetic moment $\boldsymbol{\mu}$. See Fig. 1.10 for the definition of the different vectors and angles. The probability density function (PDF) of $\theta$ is then written using Boltzmann statistics:

$$P(\theta, \phi) = \frac{e^{-E_m/kT}}{Z}, \text{ with } Z = \int e^{-E_m/kT} dV, \tag{1.13}$$

where $k$ is the Boltzmann constant, $T$ the absolute temperature and $Z$ the partition function obtained by integrating $e^{-E_m/kT}$ over all possible ($\theta$,$\phi$).

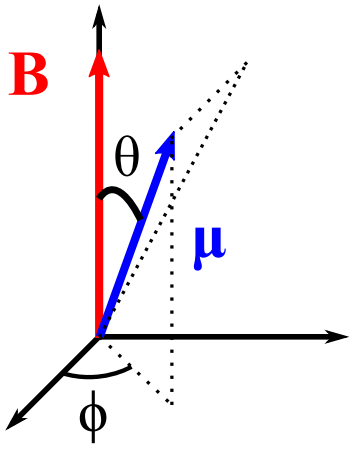


Figure 1.10: Relevant angles of interest in the paramagnetic model. $\theta$ is the angle between the magnetic moment $\boldsymbol{\mu}$ and the field $\mathbf{B}$. $\phi$ is the angle denoting the orientation of the projection of $\boldsymbol{\mu}$ in the plane perpendiculat to $\mathbf{B}$

The time-weighted average of $\cos\theta$ can be computed from the PDF and is given by:

$$< \cos\theta >= \frac{\int \cos\theta e^{-E_m/kT} dV}{\int e^{-E_m/kT} dV} = L\left(\frac{\mu B}{kT}\right), \tag{1.14}$$

where $L$ is the Langevin function given by $L(x) = \coth(x) - \frac{1}{x}$. For passively aligned bacteria swimming at $v = v_0$, the average velocity in the direction of the field is thus $v_{\parallel} = v_0 < \cos\theta >$. Frankel showed that for a typical magnetic moment $\mu = 10^{-15}$ A.m$^2$ in the geomagnetic field ($B \sim 0.5$ G), this model leads to $< \cos\theta > \sim 0.9$ and concluded that the magnetotaxis is an efficient process [40]. However, these calculations were made assuming thermal noise is the only significant source of noise. Frankel and coworkers estimated from birefringence measurements that the motility creates an additional source of non-thermal noise, which can be accounted for by replacing the absolute temperature by an effective temperature increased by 10% to 20% [41]. Recently, two groups [32, 42] estimated this effective temperature to be even higher. Additionaly, this model assumes that the magnetic moment, and thus the chain of magnetosomes, is aligned with the direction of motion. As shown in the Results section of this thesis, this should not be taken for granted.

### 1.2.3 Measuring the magnetic moment with the U-turn method

The simple model that describes MTB as self-propelled dipoles swimming at low $Re$, at a constant velocity $v_0$, has interesting implications. This section shows how the magnetic moment of MTB can be measured by analyzing their motion when the magnetic field is suddenly reversed. That technique, called the U-turn method, was used during this MSc to measure the magnetic moment of individual AMB-1 cells. If a field is applied, the dipole experiences a torque given by:

$$\mathbf{L} = \boldsymbol{\mu} \times \mathbf{B}. \tag{1.15}$$

When the field is held constant, this torque forces the cell to remain aligned with the field. However, if the field direction is suddenly reversed, the cell has to perform a U-turn to align with the new magnetic field. Using Eq. 1.11 and 1.15, one can determine

the magnetic moment of single MTB by analyzing the shape and the dynamics of this U-turn [32, 43]. The viscous drag torque applied by the field on the rotating body is $\mathbf{L}_{fluid} = -f_r \frac{d\theta}{dt}$, where $f_r$ is the rotational drag coefficient. The following differential equation is thus obtained:

$$\mu B \sin\theta = f_r \frac{d\theta}{dt}. \tag{1.16}$$

Esquivel and Lins de Barros [43] solved Eq. 1.16 to obtain the typical width for the U-turn as a function of the field, the magnetic moment and the size of the bacteria, assuming a spherical shape for the cells ($f_r = 8\pi\eta R^3$):

$$D = \frac{8\pi^2 R^3 \eta v_0}{\mu B}, \tag{1.17}$$

where $R$ is the radius of the cell and D is the width of the U-turn. If the trajectories can be recorded with a high frame rate, it becomes interesting to record the angle $\theta$ as a function of time and to use the solution to Eq. 1.16 to fit $\sin^2\theta(t)$ and thus measure the magnetic moment [32]:

$$\sin^2\theta = 1 - \tanh^2\left(\frac{\mu B(T - T_0)}{f_r}\right), \tag{1.18}$$

where $T_0$ is a temporal shift used to account for the lag between the field reversal and the beginning of the U-turn. This lag is caused by the fact that just after reversing the field, the torque experienced by the bacteria is very small ($\mu B \sin\theta << 1$ for $\theta \sim 180°$). Using Eq. 1.18 is particularly advantageous since no assumption on the velocity is required, and this equation also allows for the measurement of $\mu$ for dead cells.

## 1.3 Scanning transmission X-ray microscopy: principle and applications

As explained in 1.1.3, many questions regarding the biomineralization process in MTB remain unanswered. By identifying proteins involved in biomineralization, genetic studies have allowed for great progress to be made in understanding this complex phenomenon. However, more direct observations providing both chemical and spatial information are needed to understand how magnetosomes are synthesized and the chemical pathway of biomineralization. This section is an introduction to soft X-ray spectromicroscopy, and more particularly to the scanning transmission X-ray microscopy (STXM) technique, which was used to address some of these questions.

### 1.3.1 X-ray absorption spectroscopy

Light interacts with matter in different ways, leading to absorption, transmission or reflection of the incoming photons. When a monochromatic X-ray beam hits a sample, the photons interact with the electrons of the material through different processes, as presented in Fig. 1.11.

In X-ray absorption spectroscopy (XAS), how much the sample absorbs light at a particular energy is measured by comparing the intensity before and after the beam passes through the sample. At a particular photon energy, the amount of transmitted light depends on the thickness, the density, the elemental composition and the chemical structure of the material and is given by an equation analoguous to the Beer-Lambert law [45]:

$$I = I_0 e^{-\rho\mu x}, \tag{1.19}$$

where $I$ and $I_0$ are respectively the transmitted and incident intensities (photon flux), $\rho$ is the mass density of the material, $\mu$ is the mass absorption coefficient and $x$ is the sample thickness. For a given element, the mass absorption coefficient $\mu_{abs}$ depends both on the atomic number $Z$ and the energy of the incoming photon. Eq. 1.19 can

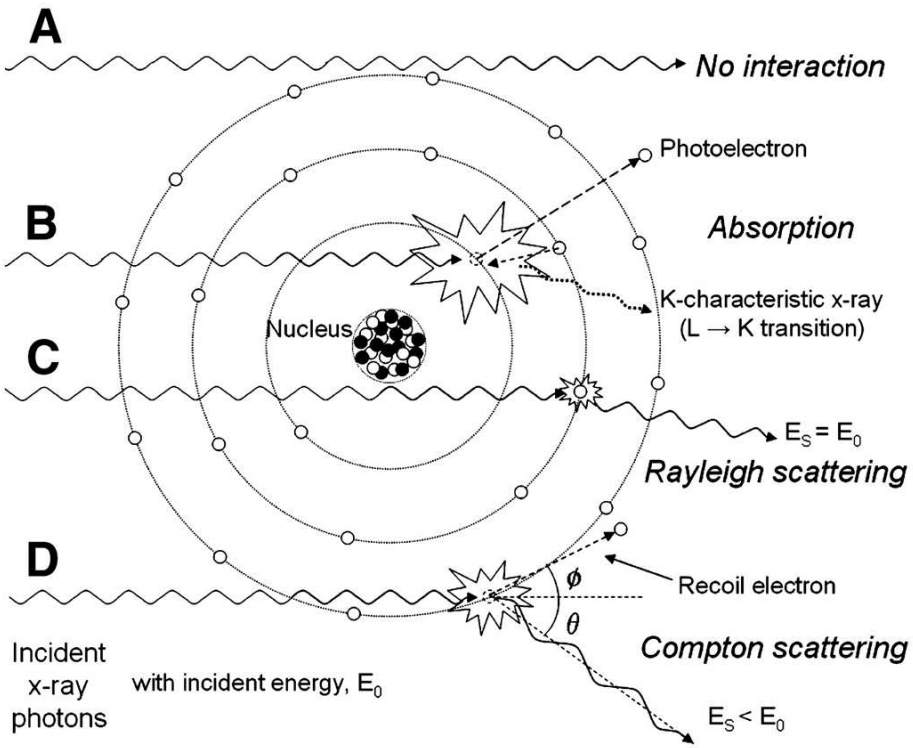


Figure 1.11: X-ray interactions with electrons. **(A)** The incoming photon does not interact with any electron, leading to unaffected transmission. **(B)** Photoelectric absorption of the photon, leading to the expulsion of an inner-shell electron (photoelectron). **(C)** & **(D)** Scattering after elastic (C) and inelastic (D) collisions. Reproduced from [44] with permission from *JNMT*.

be rewritten as a function of the atomic density $n_a$ and the absorption cross-section $\sigma_{abs}$:

$$I = I_0 e^{-n_a \sigma_{abs} x}. \tag{1.20}$$

In Eq. 1.20, $\sigma_{abs}$ depends on the energy of the incoming photon and on the atomic number. This exponential decay means that different layers in the sample will "see" a different number of incoming photons due to absorption from the other layers. The Beer-Lambert law can be derived for any homogeneous material by considering a plane wave of initial amplitude $E_0$ propagating in this material. The following derivation

is principally based on chapters 2 and 3 of [45]. Start with a wave defined by:

$$\mathbf{E}(\mathbf{r},t) = \mathbf{E}_0 e^{-i(\omega t - \mathbf{k}\cdot\mathbf{r})}, \tag{1.21}$$

The complex dispersion relation corresponding to this plane wave is:

$$\frac{\omega}{k} = \frac{c}{n}, \tag{1.22}$$

with $c = \frac{1}{\sqrt{\epsilon_0 \mu_0}}$. $\epsilon_0$ is the vacuum permittivity and $\mu_0$ is the vacuum permeability (or magnetic constant). The complex refractive index for soft X-rays is close to unity and can be written as:

$$n = 1 - \delta + i\beta. \tag{1.23}$$

Using Eq. 1.22 and Eq. 1.23, Eq. 1.21 can be rewritten, in the direction of propagation defined by $\mathbf{k}\cdot\mathbf{r} = kr$, as:

$$\mathbf{E}(\mathbf{r},t) = \mathbf{E}_0 e^{-i\omega(t-r/c)} e^{-i(2\pi\delta/\lambda)r} e^{-(2\pi\beta/\lambda)r}, \tag{1.24}$$

where $\lambda$ is the wavelength of the propagating wave. The last exponential term in Eq. 1.24 represents the attenuation of the wave amplitude. To calculate the intensity, one must first know the expression of the magnetic field associated with the studied plane wave. The following relation is obtained between $\mathbf{k}$, $\mathbf{E}$ and the magnetic field $\mathbf{H}$ by working on the Maxwell-Faraday equation in the case of a propagating plane wave:

$$i\mathbf{k} \times \mathbf{E} = i\omega\mu_0 \mathbf{H}. \tag{1.25}$$

Using Eq. 1.25 and the dispersion relation, and writing $\mathbf{k} = k\mathbf{k}_0$ with $\mathbf{k}_0$ a unit vector pointing in the direction of light propagation, the magnetic field can be written as:

$$\mathbf{H}(\mathbf{r},t) = n\sqrt{\frac{\epsilon_0}{\mu_0}}\mathbf{k}_0 \times \mathbf{E}(\mathbf{r},t). \tag{1.26}$$

Finally, the average intensity can be obtained by computing the magnitude of the time-averaged Poynting vector:

$$I = \frac{1}{2} \mid Re(\mathbf{E} \times \mathbf{H}^*) \mid = \frac{1}{2} Re(n) \sqrt{\frac{\epsilon_0}{\mu_0}} \mid \mathbf{E} \mid^2 . \tag{1.27}$$

Using Eq. 1.24, Eq. 1.27 can be rewritten as:

$$I = I_0 e^{-(4\pi\beta/\lambda)r}, \tag{1.28}$$

which corresponds to the Beer-Lambert equation. It is thus possible to relate the mass absorption coefficient $\mu$ to the parameter $\beta$. Further calculations can show that $\beta$ itself is a function of the imaginary part of the forward atomic scattering factor, which is tabulated and is element, bonding and energy dependent.

For any material, the transmitted intensity thus decays exponentially with the thickness of the sample. But for a given material and a given sample thickness, the amount of transmitted light highly depends on the energy of the incoming beam, which we assume to be monochromatic. The following discusses only the absorption phenomenon. In general, high energy photons are more penetrating than low energy photons, which causes the absorption to generally decrease with increasing energies. This can be seen in the tabulated mass absorption coefficient, as presented in Fig. 1.12.

As the energy increases, the photons exceed the threshold needed to excite (transition to higher energy levels) or ionize (expulsion of the electron) electrons in the material. These processes give rise to the so-called absorption edges, at which the absorption suddenly increases due to the photon energy becoming larger than the threshold energy needed to excite the core-shell electrons. These edges are named after the shell being excited: the $K$ edge corresponds to excitation of the $1s$ electrons (Fig. 1.12),

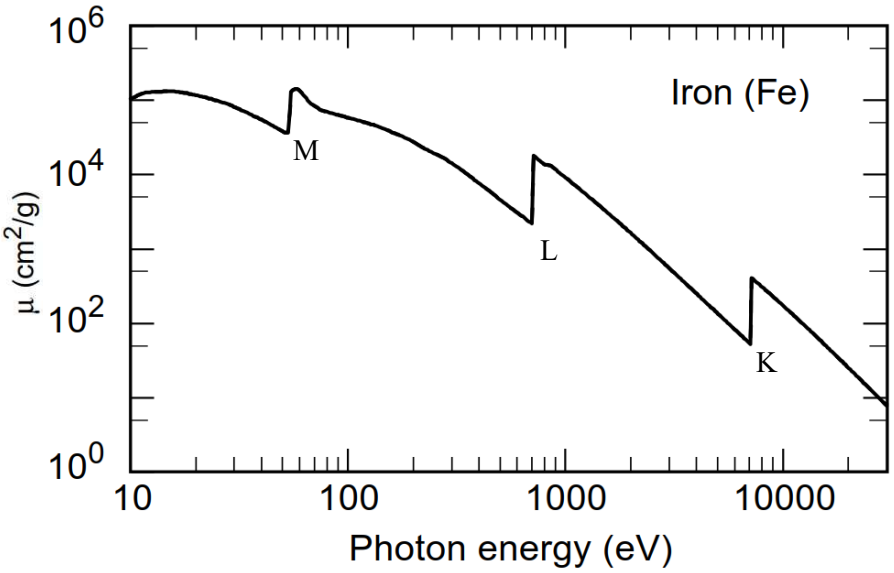


Figure 1.12: Mass absorption coefficient of iron as a function of energy. Absorption decreases with energy, except at some specific energies corresponding to absorption edges, indicated by the letters K, L and M. Adapted from [46].

the $L$ edge to the $2s$ ($L_1$ edge) and $2p$ ($L_2$ and $L_3$ edges) electrons, etc.

The energy of a given edge increases monotonically with the atomic number. Each inner-shell level of each element has a characteristic edge energy. But this description is only an approximation, as it does not take into account the electronic fine structure at each edge due to factors such as spin-orbit coupling, crystal field, atomic multiplets and the effect of surrounding atoms. The high energy resolution available in the soft X-ray domain allows one to probe this near edge X-ray absorption fine structure (NEXAFS). For iron oxides such as magnetite, the fine structure and degree of oxidation can be conveniently studied at the $L_3$ and $L_2$ edges between 700 and 730 eV, where the absorption spectra exhibit structured peaks separated by 13 eV corresponding to resonant transitions from the ground state to many states arising from the ($2p^{-1}$, $3d^{+1}$) configuration. Changes in chemical composition and/or degree of oxidation lead to different spectra, as shown in Fig. 1.13. The absorption is usually plotted in terms of optical density (OD):

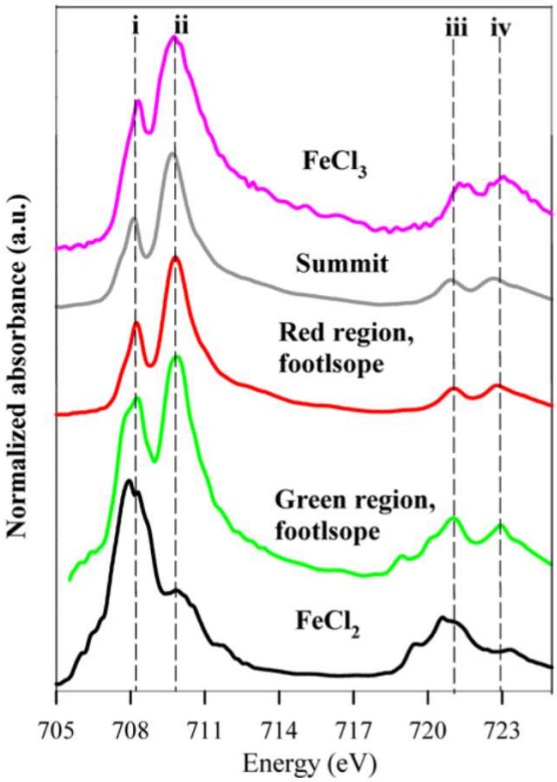


Figure 1.13: NEXAFS of $FeCl_3$ (pink), $FeCl_2$ (black) and various environmental soil samples containing iron species (green, red, grey). Reproduced from [47]. Copyright (2014) *American Chemical Society*.

$$OD = ln\left(\frac{I_0}{I}\right), \tag{1.29}$$

### 1.3.2 X-ray magnetic circular dichroism

Magnetosomes are single-domain magnetic nanoparticles, and therefore their magnetic properties can be studied with X-rays. Because of the ferromagnetic properties of iron, the way magnetite absorbs X-rays depends on the polarization of the incoming beam. The X-ray magnetic circular dichroism (XMCD) technique uses left-circularly polarized (LCP) and right-circularly polarized (RCP) light to probe the spin state in the partially filled $3d$ shell. This technique can be used to determine the orientation of a magnetic moment, and also to calculate the magnitude of the spin and orbital

contributions to the magnetic moment through the use of specific sum rules [48].

The XMCD signal is obtained by subtracting the XAS obtained with RCP light from the XAS obtained with LCP light, with RCP and LCP defined using the point of view of the source. In the case of a magnetic material made of iron, such as magnetosomes, two clear signals appear at the $L_2$ and $L_3$ edges. The existence of the XMCD contrast can be explained by a 2-state model proposed by Stöhr that is briefly detailed here [48]. Consider an atom, such as iron, where the $3d$ shell is not fully occupied. There is therefore an imbalance between the number of spin-up and spin-down electrons in the $3d$ valence shell (Fig. 1.14). The magnetization $m$ is assumed to be in the "up" direction, which means that there are more spin-down than spin-up electrons. We also assume this magnetization to be collinear to the direction of light propagation.

The first step of the model considers the probability for interaction between a $2p$ electron with RCP or LCP photons. RCP and LCP photons possess opposite spin angular momentum ($q = +1$ and $q = -1$ respectively along the direction of light propagation, in the unit of $\hbar$), which makes each polarization interact preferentially with either spin-up or spin-down electrons of the $2p$ level depending on the edge, due to spin-orbit coupling. At the $L_3$ edge, RCP light interacts at 62.5% (resp. 37.5% for LCP) with spin-up and 37.5% (resp. 62.5% for LCP) with spin-down electrons. Due to opposite spin-orbit coupling, the opposite behaviour is obtained at the $L_2$ edge (RCP interacts more with spin-down electrons). In the absence of an imbalance between spin-up and spin-down electrons, the transition probabilities are the same for exciting spin-up and spin-down $2p$ electrons and thus the absorption spectra measured with RCP and LCP are the same. But in the case of a ferromagnetic atom with more spin-down than spin-up electrons, the density of accessible states is modified and the transition probability for $2p$ spin-down electrons is decreased. At the $L_3$ edge, LCP interacts more with spin-down electrons than LCP. Therefore LCP light is less absorbed than RCP light for this transition. At the $L_2$ edge the preferential interactions are opposite, causing RCP light to be less absorbed than LCP light. These polarization-dependent differences in absorption are the origin of the XMCD signal, which is obtained by taking the difference between the LCP and RCP XAS:

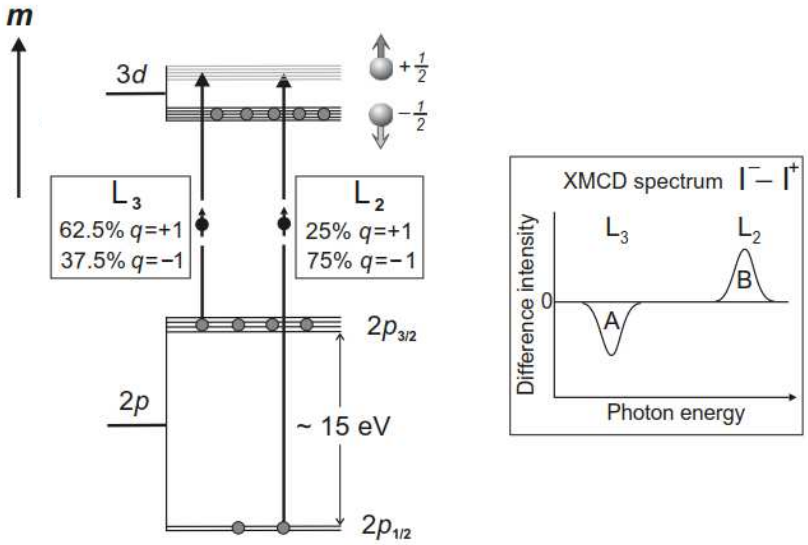


Figure 1.14: XMCD principle: two-state model. A simplified atomic model is considered on the left. The atom is in a magnetization-up state, with the $3d$ spin-down entirely filled. The magnetization is assumed to be parallel to the incoming X-ray beam. At the $L_3$ edge, RCP ($q = +1$) interacts preferentially with spin-up electrons, while LCP ($q = -1$) interacts more with spin-down electrons. Since no additional spin-down electrons can be added to the $3d$ level, the absorption of LCP light is decreased compared to RCP absorption. The XMCD signal is obtained by subtracting RCP absorption from LCP absorption ($I_{XMCD} = I^- - I^+$), and a negative peak is therefore obtained at the $L_3$ edge. The opposite behaviour is obtained at the $L_2$ edge. Adapted from [48] with permision from *Springer*.

$$I_{XMCD} = OD_{LCP} - OD_{RCP} \tag{1.30}$$

To obtain an XMCD signal, the projection of the magnetic moment (and thus of the magnetosome chain) on the beam direction needs to be different from zero. Otherwise, there cannot be preferential absorption for LCP or RCP. Since the magnetic moment of the magnetosome chain is in the plane of the cell, the sample must be tilted with respect to the X-ray propagation direction. Kalirai and coworkers [51] used XMCD to probe the orientation of the magnetic moment in MTB species MV-1 (opposite polarities are characterized by opposite XMCD signals) and showed that

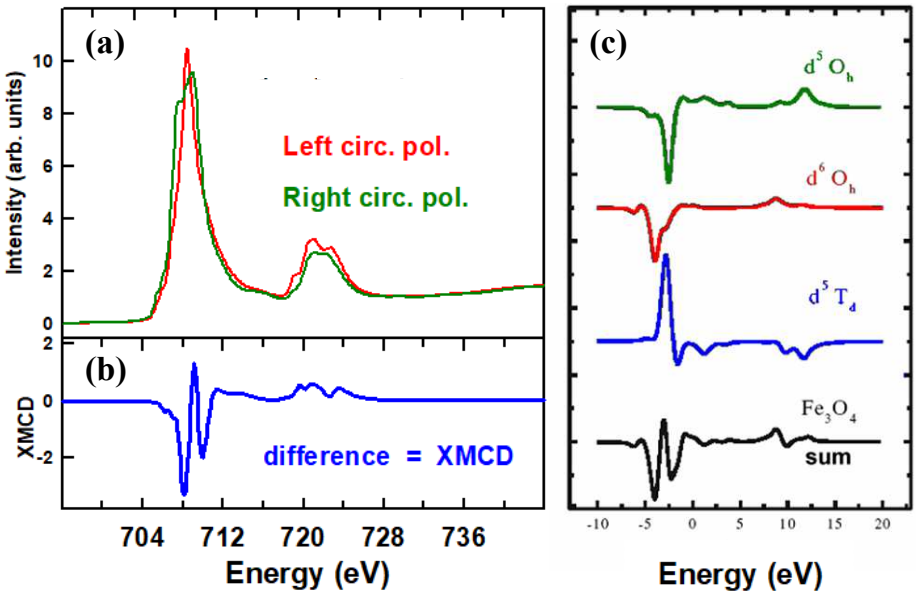


Figure 1.15: XMCD signal of magnetite. **(a)** X-ray absorption spectra of magnetite with LCP and RCP. **(b)** XMCD signal obtained by taking the difference of the two spectra presented in (a). **(c)** Fe(II, $O_h$) (red), Fe(III, $O_h$) (green) and Fe(III, $T_d$) (blue) calculated XMCD contributions to the XMCD signal of magnetite. (a) and (b) are adapted from [49]. (c) is adapted from [50].

the subchains that constitute the magnetosome chain do not always point in the same direction. As shown in Fig 1.15, the XMCD signal of magnetite is complex, due to the presence of Fe in three different symmetry sites and oxidation states; Fe(II, $O_h$), Fe(III, $T_d$), Fe(III, $O_h$).

### 1.3.3 STXM operating principles

Scanning transmission X-ray spectroscopy (STXM) is a synchrotron-based technique that can provide chemical and magnetic mapping through the measurement of spatially resolved X-ray absorption spectra. X-rays are generated by electrons accelerated in the storage ring of the synchrotron facility, and go to a monochromator that selects the desired wavelength and thus energy (Fig. 1.16). The beam of X-rays is then focused on the sample by a Fresnel zone plate (ZP) and the transmitted intensity is measured by a detector [52].

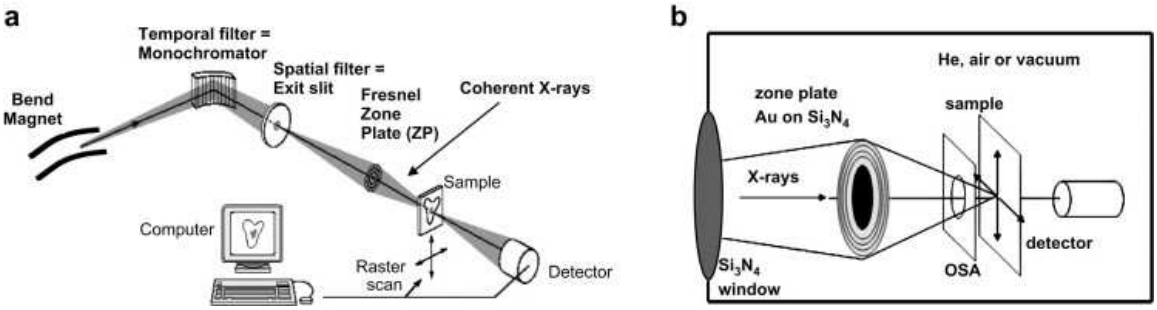


Figure 1.16: Schematic of a scanning transmission X-ray microscope (STXM). **(a)** Schematic of the beamline. **(b)** Schematic of the inside of the STXM chamber. Reproduced from [52] with permission from *Elsevier*.

The Fresnel ZP uses diffraction to focus the X-ray beam and is made of concentric circular zones, which alternate between transparent and opaque, and have decreasing width as they get further away from the ZP center. The best spatial resolution achievable with such optics is given by:

$$\Delta l = 1.22 \cdot \Delta r_n, \tag{1.31}$$

where $\Delta l$ is the best achievable resolution and $\Delta r_n$ is the width of the outermost zone of the ZP. State of the art ZP can achieve approximately 10 nm resolution [53] whereas most facilities use ZP with 20-30 nm spatial resolution on a routine basis.

Raster scanning of the sample at the focal point of the ZP at a given energy provides an image based on the transmitted intensity recorded for each pixel, which can then be converted to OD using a suitable $I_0$. A stack of images can be recorded by repeating this process at multiple energies, leading to the acquisition of an X-ray absorption spectrum for each pixel. With an energy resolution of less than 0.1 eV, STXM is a suitable tool for probing the electronic fine structure of the studied compounds. Since the polarization of the incoming X-rays can be controlled and alternated between RCP and LCP, XMCD measurements can also be performed. As a spectromicroscopy technique, STXM can thus be used to map the different chemical species and magnetic

domains within a sample by comparing the absorption spectra or XMCD signals obtained for each pixel. Comparing measured signals to experimental and theoretical reference spectra can allow one to identify and locate the chemical species contained in the sample.

# Chapter 2

# Experimental Methods

## 2.1 Cultivation of MTB strain AMB-1

MTB strain AMB-1 is grown in both iron-rich and iron-depleted conditions. Iron-rich conditions are used to grow bacteria for the optical microscopy study focused on measuring the orientation of the magnetic moment with respect to the cell axis. Iron-depleted conditions are used to obtain a non-magnetic culture, *i.e.* a culture with cells producing only a very low number of magnetosomes. Both cultures are grown in a liquid medium with controlled $O_2$ conditions, at 32°C. Cultures are transferred into fresh medium every 3 to 6 days.

A paper (not included in this thesis) describing a detailed protocol for growing MTB was written during this MSc and accepted for publication in the *Journal of Visualized Experiments* [54].

### 2.1.1 Iron-rich medium

The iron-rich liquid medium contains, per liter of medium: 1.0 mL modified Wolfe's mineral elixir [55, 56], 0.1 g $KH_2PO_4$, 0.15 g $MgSO_4{\cdot}7H_2O$, 2.38 g HEPES, 0.34 g $NaNO_3$, 0.1 g yeast extract, 3.0 g BD Bacto Soytone, 4.35 mL potassium lactate (60% solution) and 5 mL Fe (III) citrate sterile 10 mM stock solution. The pH is adjusted to 7 and dissolved $O_2$ is removed by bubbling $N_2$ in the medium. The medium is autoclaved at the end of the preparation process to ensure sterility. $O_2$ is

added in the culture flasks before inoculation (1.5 % concentration in the headspace).

### 2.1.2 Iron-depleted medium

The iron-depleted liquid medium contains, per liter of medium: 0.1 g $KH_2PO_4$, 0.15 g $MgSO_4 \cdot 7H_2O$, 2.38 g HEPES, 0.34 g $NaNO_3$, 1.0 g BD Bacto Soytone and 4.35 mL potassium lactate (60% solution). The pH is adjusted to 7 and dissolved $O_2$ is removed by bubbling $N_2$ in the medium. The medium is autoclaved at the end of the preparation process to ensure sterility. $O_2$ is added in the culture flasks before inoculation. Results presented in this thesis were obtained with a culture exposed to 5% $O_2$ in the headspace. Cultures exposed to 23% $O_2$ are currently being tested for future experiments.

### 2.1.3 The racetrack method

In nature, bacteria that are unable to perform chemotaxis and/or magneto-aerotaxis are likely to die since they cannot migrate towards favorable conditions. The iron-rich medium provides highly favorable growth conditions to the bacteria. As a result, bacteria that experience mutations affecting their motility or their ability to produce magnetosomes do not necessarily die. The culture thus progressively evolves and can spontaneously lose its motility or magnetism.

The race-track method [57], originally developed to isolate MTB from environmental samples, provides a way to recover a magnetic and motile culture. This method is based on the assumption that even if most cells have lost their magnetism and/or motility, some of them still possess both properties.

To perform the race-track, a glass pipette is sealed at its thinner end by melting the glass in the flame of a bunsen burner. A small piece of sterile cotton is placed inside the pipette, to act as a filter. The pipette is then filled with fresh, sterile medium up to the cotton filter. A small volume of the MTB culture is added at the larger end of the pipette. The pipette is then kept horizontal, with the South pole of a magnet placed at the sealed end. MTB that are both magnetic and motile can go

through the cotton filter and swim towards the magnet, accumulating at the sealed end of the pipette. After approximately 30 min, the tip of the pipette is broken and the content is transferred into fresh medium using a sterile syringe. This method was used 4 times during this MSc.

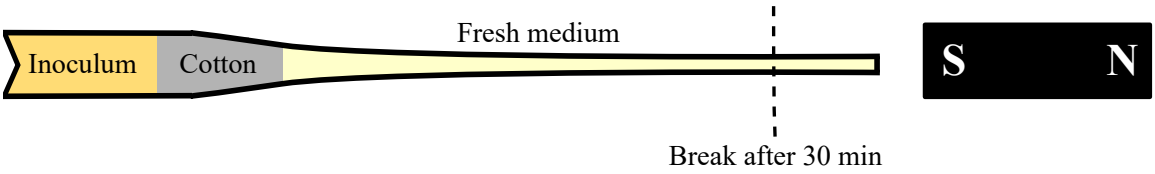


Figure 2.1: Illustration of the race-track method. Cells are allowed to swim towards the tip of the sealed pipette for 30 min before the tip is broken. Cells are then harvested and transfered into a flask of growth medium. Only cells that are both motile and magnetic can reach the tip of the pipette.

## 2.2 Optical microscopy measurements in a controlled magnetic field

Experiments to study the orientation of the magnetosome chain with respect to the cell axis are principally conducted using phase contrast optical microscopy, in a controlled magnetic field. The U-turn technique is also based on optical microscopy.

### 2.2.1 Experimental setup

Experiments are performed using a Nikon Eclipse E200-LED upright microscope, modified to fit a pair of custom-made Helmotz coils, each made of 300 loops of copper wire (0.06 $mm^2$ wire cross-section). The radius of the coils radius is 3.6 cm and the spacing between them is 4 cm. The pair of Helmotz coils is reinforced by two iron cores placed at the center of each coil. A controlled magnetic field is generated by passing square waves of known voltage and frequency through the coils, using an Agilent 33120A power supply connected to an Agilent 33502A amplifier. The coils are calibrated (Fig. 2.2) each time the setup is modified, (*e.g.* after moving the whole

setup or the iron cores), using a DC Gaussmeter (AlphaLab Inc). The cores are cautiously positioned to ensure that the field is symmetric, i.e. that the absolute value of the field remains the same when the field is reversed.

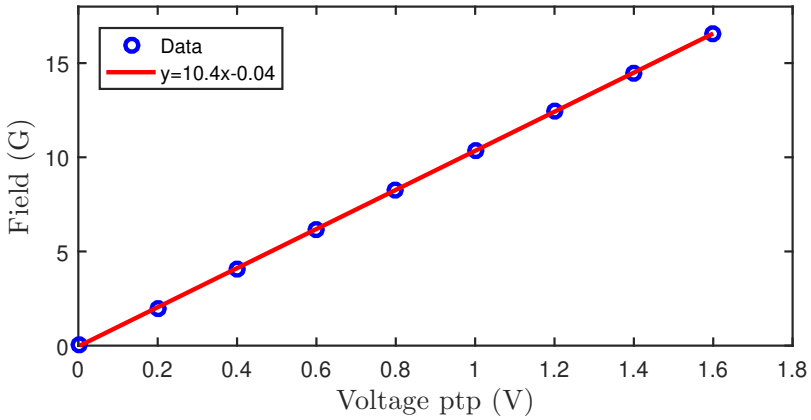


Figure 2.2: Helmotz coils calibration. Blue circles are obtained by averaging the two values of the field obtained for positive and negative intensity circulating through the coils. Error bars are smaller than the data points and thus omitted. Red line is the calibration curve, resulting from a fit of the data. The intercept is not forced to zero to show that the best fit is actually very close to a straight line passing through the origin.

Bacteria are studied with a 40x phase contrast objective, and movies are recorded with a Prosilica GE (Allied Vision) camera at 100 frames per second, using the Streampix 5 software. Thin custom-made observation chambers are prepared by melting two strips of parafilm between a glass slide and a coverslip. MTB are harvested from the culture and killed by heating the aliquot to 50°C for 15 min. The solution of dead bacteria is then diluted to a low concentration with fresh medium, and introduced in the thin chamber, which is subsequently sealed with vacuum grease to prevent evaporation and flow inside the chamber.

Experiments can be performed with magnetic field magnitudes ranging from 2 G to to 30 G. Experiments performed to determine the orientation of the magnetic moment with respect to the cell axis are performed in a constant field. U-turn experiments on dead cells are performed in an alternating magnetic field of frequency 500 mHz.

### 2.2.2 Image analysis

Optical microscopy movies of MTB are analyzed using codes I have written in MATLAB during this MSc. Two similar tracking codes were written. For each frame, the first step is to binarize the image using a local adaptive threshold. After selection of a region of interest (ROI) around a cell by the user, dark pixels that constitute the cell are detected and saved. Two methods can then be used to determine the orientation of the cell: the cell is either fitted to an ellipse or to a sinusoidal curve. In both cases, the angle between the cell and the magnetic field is obtained for each frame. Other parameters, such as the length of the cell and its position, are also recorded. The ROI is automatically moved between successive frames, based on the displacement of the cell centroid detected in the two preceding frames. This functionality has been tested on swimming MTB and provides statisfactory tracking results. However, these programs do not detect collisions between cells, and do not automatically remove dark pixels coming from dust particles or other bacteria in the ROI. These codes thus require clean, dilute samples to work properly.

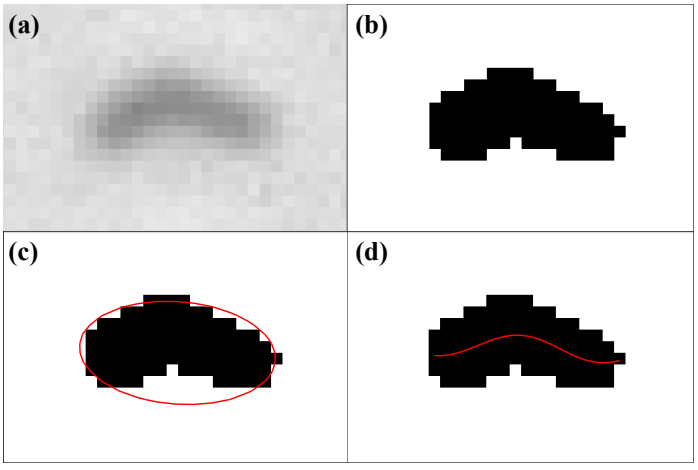


Figure 2.3: Ellipse vs sine fit. **(a)** Original grayscale of an AMB-1 cell observed with 40x phase contrast. **(b)** Thresholded image. **(c)** Cell fitted to an ellipse. **d** Cell fitted with a sine function.

### Ellipse fit

The fit to an ellipse is done by finding the smallest ellipse that encloses all the pixels (Fig. 2.3 (a)-(c)). The minimization algorithm used in this tracking program is adapted from the MinVolEllipse function written by Nima Moshtagh (Minimum Volume Enclosing Ellipsoid, Nima Moshtagh, version 1.2.0.0). The orientation of the cell is then obtained by measuring the angle between the long axis of the ellipse and the horizontal direction.

### Sine fit

The fit to a sine function is mathematically simpler than the ellipse fit, but computationaly more costly. The orientation of the cell is first roughly estimated from a least squares fit of the cell to a straight line. The cell is moved to the origin and rotated by the angle $\theta_{line}$ measured with the line fit to make it approximately horizontal. The pixels that constitute the cell are then binned vertically to obtain the "backbone" of the cell, which is fitted to a sinusoidal function, $y = A\sin(\omega x + \phi)$. The error associated with this fit is recorded, and the whole process is repeated, starting from the rotation step, for rotation angles ranging from $\theta_{line} - 8°$ to $\theta_{line} + 8°$ with $1°$ steps. The angle returning the smallest error for the fit is recorded, and angles within $\pm 0.5°$ of this angle are also tested. At the end, the orientation of the cell is given by the rotation angle that leads to the smallest error.

Fitting the cell to a sinusoidal function is valid because the cells are helical in morphology and the angle between the cell axis and the focal plane remains small throughout the experiment. The cell thus presents a sinusoidal 2D projection in the focal plane. As explained in the manuscript presented in the Results section of this thesis, the sine fit is advantageous because it gives access to additional geometrical parameters, such as the phase of the sinusoidal function. However, one limitation of this method is the significant computational cost, since 19 fits and rotations are performed for each frame in movies that contain in average several thousands of frames.

### 2.2.3 Data analysis

The tracking algorithms presented in 2.2.2 provide the angle between the cell and the field as a function of time, as well as geometrical parameters such as the cell length, or the amplitude and the phase of the sinusoidal function for the sine fit method. Three types of analysis are performed:

1. For movies recorded with an alternating magnetic field, the angle is obtained with the ellipse fit. The U-turns are studied by plotting $\sin^2\theta$ as a function of time, and by fitting the peaks obtained for each U-turn with Eq. 1.18 (Fig 2.4). The value of the rotational drag coefficient $f_r$ is calculated from the cell length, based on a relationship experimentally obtained by previous students in the group (unpublished data): $f_r = 2.9 \times L^{2.7}$, where L is the cell length in $\mu$m and $f_r$ is expressed in fN.$\mu$m.s.

2. Movies recorded with a constant field are analyzed with the sine fit method. The angle is plotted as a function of the phase of the sine function used to fit the cell. If the magnetic moment is aligned with the cell axis, the same distribution of angles, centered at zero, should be obtained for all values of the phase. However, if a misalignment exists between the magnetic moment and the cell axis, a correlation between the phase and the cell orientation should be obtained. Plotting the cell orientation as a function of the phase thus provides a way to measure the potential misalignment between the cell and its magnetic moment. The theory developed during this MSc to perform this measurement and the consequences of a misalignment are detailed in the manuscript presented in the Results section.

3. The only angle directly accessible from optical microscopy is the cell orientation. To obtain the magnetic moment orientation distribution, the cell orientation distribution must be corrected by subtracting from each measured angle a phase-dependent angle calculated as a function of the measured misalignment. Once the correct histogram is obtained, Eq. 1.13 can be used to fit it and estimate the magnetic moment.

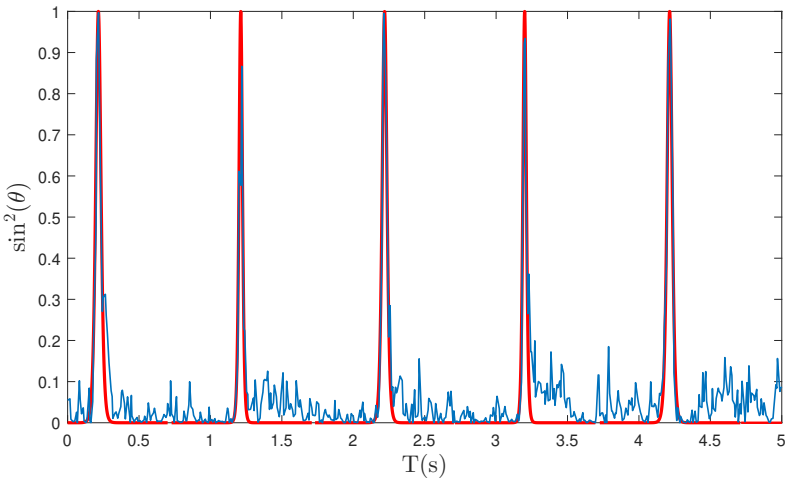


Figure 2.4: Typical U-turn data. Blue line is the experimental data, obtained with an alternating field (500mHz, 10G). Red line is a fit obtained with Eq. 1.18, returning a magnetic moment $\mu = 1.7 \times 10^{-15}$A.m$^2$ for the specific cell presented here.

## 2.3 Transmission electron microscopy

Transmission electron microscopy (TEM) is used to record high-resolution, high-magnification images of MTB. It allows for a direct observation of the magnetosomes and of the cell morphology, and is thus useful to verify that the bacteria are growing as expected. Samples are prepared by depositing a droplet of MTB culture onto a formvar-coated TEM grid. Cells are allowed to settle for 10 min, then the excess liquid is removed with small pieces of tissue wiper. Samples are imaged using a JEOL 1200EX TEMSCAN microscope.

In this work, TEM is used mostly to provide another way of measuring the misalignment between the cell axis and the magnetic moment. For each cell, the position and volume of each magnetosome is obtained by manual analysis using ImageJ. The magnetosome chain is then divided into linear segments. The magnetic moment of each subchain is assumed to be aligned with the axis of the subchain. Each subchain's orientation is determined by performing a linear least squares fit of the coordinates of the magnetosomes constituting the subchain. Once the orientations of all segments are known, the orientation of the total magnetic moment is calculated as the

volume-weighted average of these orientations. Each subchain thus contributes proportionally to the volume of magnetic material it contains. The orientation of the cell is then measured using the sine fit method, with a code adapted from the one described in 2.2.2. The magnetic moment of a cell can be estimated by multiplying the measured volume of magnetic material by the saturation magnetization of magnetite ($M_{sat} = 4.8 \cdot 10^{-22} A.m^2.nm^{-3}$ [58]). Since the magnetosomes are SD particles, each magnetosome is indeed likely to have a magnetization close to the saturation magnetization. This was experimentally confirmed by Kalirai and coworkers, who reported a magnetic moment equal to 90% of the saturation magnetic moment in two cells of the species MV-1 [59]. However, calculations based on the saturation magnetization remain an approximation since the magnetosome chain is not a perfect straight line and all subchains do not point in the exact same direction. The contribution of each subchain is thus reduced compared to the one expected from the case with all magnets saturated and in a straight line.

## 2.4 Time-course studies with X-ray absorption spectroscopy

STXM is used in this work principally to study the biomineralization process in MTB. Time-course samples are first prepared at McMaster and then imaged at the synchrotron facilities. Measurements on AMB-1 cells cultured in iron-rich medium are also performed to serve as a reference.

### 2.4.1 Time-course cultures

A non-magnetic culture is obtained after several transfers in iron-depleted medium. The magnetism is regularly checked with optical microscopy (by observing how the cells align in the field) and TEM (to estimate the number of magnetosomes per cell). Once the culture is non-magnetic, 30 mL of the non-magnetic culture is transferred into 30 mL of fresh iron-rich medium to induce biomineralization. This transfer marks the beginning of the time-course. The same culture bottles as for regular cultures are used and the $O_2$ concentration is controlled (1.5% in the headspace). At specific times

(*i.e.* after 10 min, 30 min, 1 h, ... 48h), aliquots are extracted from the culture and heated to 50° for 15 min to kill the bacteria and stop the biomineralization process. Aliquots are then stored at 4°C.

### 2.4.2 Sample preparation for STXM measurements

Samples are prepared by depositing a droplet of MTB culture onto a TEM grid. Cells are allowed to settle for 10 min, then the excess liquid is removed with small pieces of tissue wiper. Grids are previewed with TEM to identify the regions of interest. Grids are then mounted on STXM plates, as shown in Fig. 2.5, with small pieces of tape. Regular XAS is performed with flat plates, while XMCD measurements require the use of a holder tilted by an angle of approximately 30°.

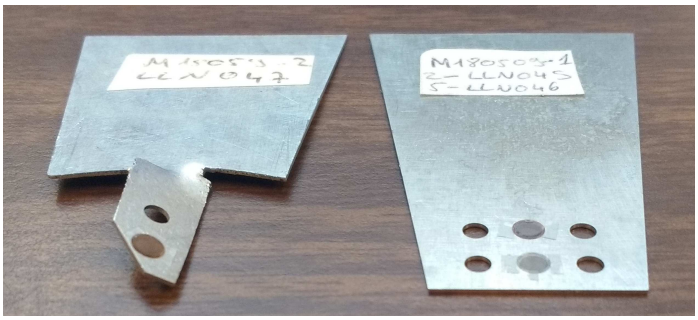

Figure 2.5: XMCD (left) and regular XAS (right) STXM plates. Grids are held in place on top of the holder's holes with small pieces of tape.

Salts and organic compounds present in the growth medium can alter the image and spectral quality, as they tend to cover the MTB cells on the grid and thus contribute to the absorption. For strong signals (*i.e.* for mature magnetosomes) this is not an issue, but weak signals such as small, growing magnetosomes or intracellular iron, can be completely dominated by the absorption of these undesired compounds. This is thus an issue for time-course samples, for which the goal is to study the spectroscopy of growing magnetosomes and iron species present in the cytoplasm. Two methods have been tested to prepare cleaner samples:

1. After deposition and drying of a droplet of culture on the grid, a droplet of

deionized water is deposited on the grid. Some of the salts and organic compounds dissolve in the water, which is then dried out with small pieces of tissue wiper. This method is interesting for its simplicity, but reproducibility is not guaranteed.

2. A second method tested is to fix the cells with a 2% glutaraldehyde solution. Unlike unfixed cells, fixed cells can be redispersed in deionized water without being lysed. This method provides perfectly clean samples, however the impact of the fixating agent on the intracellular dissolved iron is not known. This method is thus not suitable if the cytoplasmic iron needs to be studied, but is interesting if the main goal is the spectroscopy of growing crystals.

### 2.4.3 Data acquisition and analysis

Samples are studied at ambient temperature on the STXM beamline at the Canadian Light Source (CSL, Saskatoon, Canada), and on the HERMES beamline at the SOLEIL synchrotron (Saint-Aubin, France). After positioning the sample in the STXM chamber, the air present in the chamber is evacuated and replaced with Helium (CLS) or the tank is pumped throughout measurement (Soleil). After optimization of the beam and focusing on the region of interest, magnetosomes are studied at the Fe $L_3$ edge: stacks of images are recorded between 700 eV and 715 eV, with typical energy steps of 0.2 to 0.5 eV between consecutive images and typical pixel size of 15 nm to 30 nm.

Regular XAS is performed using a single light polarization (either LCP or RCP). For XMCD measurements, the sample is scanned twice at each energy, once with each polarization. In each image, each pixel is characterized by a transmitted intensity. The signal-to-noise ratio can be improved by increasing the amount of time spent on each pixel (typical dwell time of 1-2 ms for navigation in the sample and quick studies, $\sim$10 ms for fine analysis).

The analysis is performed using the aXis2000 software (available for free at unicorn.mcmaster.ca/aXis2000.html). For a given stack, the spatial drift that is likely to occur during acquisition (which can take more than six hours) is corrected by an

alignment algorithm. Transmitted intensity is then converted to OD using Eq. 1.29. $I_0$ is usually measured internally, *i.e.* on a region of the stack that does not contain sample (away from the studied cell). Absorption spectra can then be extracted from regions of interest. The software provides a fitting algorithm that allows for mapping different species in the sample. The absorption spectrum of each pixel is fitted by a linear combination of a set of reference spectra chosen by the user. These reference spectra can be spectra measured independently on known compounds, but could also be spectra isolated directly in the sample being studied.

# Chapter 3

# Results & Discussion

This chapter presents the experimental results acquired during this MSc. The first section presents measurements of the magnetic moment performed on individual bacteria using the U-turn method. These experiments were performed at different magnetic field strengths to investigate the relationship between magnetic moment and magnetic field. Results show that at low fields (2-30 G), the magnetic moment is constant. In the second section, the draft of a paper written during this MSc is included and the contributions of the different co-authors are discussed. The goal of the experiments presented in this paper draft was to study the orientation of the magnetic moment with respect to the cell axis in individual MTB. The results obtained from this work demonstrate the existence of a misalignment in a significant number of cells and show that this misalignment needs to be accounted for in order to perform a non-biased measurement of the magnetic moment from statistical methods. In the last section, magnetosome production by AMB-1 is studied in a time-course study. AMB-1 cells were initially grown in an iron-depleted medium, to prevent them from producing magnetosomes. This non-magnetic culture was then transferred into fresh medium containing a major source of iron to induce biomineralization. Cells sampled at different stages in the time-course experiment were studied with STXM, to investigate how iron absorbed by the cell is brought to the growing magnetosomes and converted to magnetite. This chapter is thus focused on magnetosomes in the AMB-1 species, from crystal formation to the chain arrangement that confers to the cell a permanent magnetic moment, more or less aligned with the cell axis.

## 3.1 Magnetic moment measurements with the U-turn method

In order to study the relationship between the magnitude of the magnetic moment $\mu$, the magnitude of the magnetic field B and the cell length, 21 AMB-1 cells were studied in alternating magnetic fields using the U-turn method. For 13 bacteria, at least two measurements at different magnetic field amplitudes were performed. For the others, only one data point was recorded before the cell went out of the field of view. The graph of the magnetic moment as a function of the magnetic field shows no particular correlation between those quantities (Fig. 3.1 (a)). Among the cells for which multiple data points are available (Fig. 3.1 (a), solid and dash lines) some bacteria exhibit an increasing magnetic moment with the field, some others a decreasing moment, and in some cases the moment does not change. This indicates that the magnetic moment of each cell can be considered constant over the range of magnetic fields used in the experiments presented in this thesis (B$\leq$30 G). It also shows that some uncertainty is present in the measurement, even if several (at least 5) U-turns are analyzed for each cell at a given magnetic field amplitude.

Fig. 3.1 (b) presents the magnetic moment of each bacteria as a function of the cell length, for all 21 cells tested. A positive correlation is obtained, indicating that longer cells possess more magnetosomes and thus a larger magnetic moment. The correlation is weak ($R^2 = 0.4$), but this is expected for a biological sample. This positive correlation is confirmed by results presented in section 3.2, obtained with a different method.

The U-turn technique is thus a useful technique for measuring the magnetic moment of MTB. It can be used routinely once an appropriate tracking and fitting algorithm has been developed. However, this method requires an accurate value for the rotational drag coefficient. For rod-shaped bacteria and ellipsoids, mathematical models are available to calculate this drag coefficient based on the size of the cell. For more complicated geometries such as spirilla, the drag coefficient needs to be determined experimentally first.

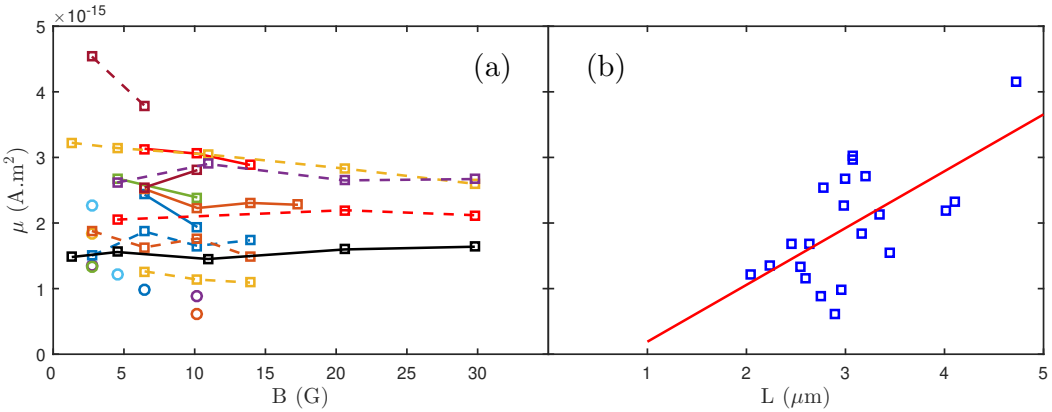


Figure 3.1: Magnetic moment measurement with the U-turn technique. **(a)** Magnetic moment versus field magnitude for 21 cells. Square markers linked by solid and dash lines are multiple measurements carried out on the same cell. Circles correspond to bacteria for which only one data point is available. **(b)** Relationship between the magnetic moment and the cell length. Red solid line is a linear fit to the data, returning a coefficient of determination $R^2 = 0.4$.

## 3.2 Misalignment between magnetic moment and cell axis in AMB-1

In this section, the reader will find a paper draft that contains the results of experiments performed to investigate the orientation of the magnetic moment relative to the cell axis. Analysis of the experimental results shows that a misalignment exists and needs to be taken into account when measuring the orientation distribution of AMB-1 in an external field.

This study was designed by Cécile Fradin and the setup for optical microscopy measurements was created by Cécile Fradin and Solomon Barkley before the beginning of this MSc, for a different project. Bacteria were grown at McMaster by me, using techniques demonstrated by Dennis Bazylinski at the beginning of this MSc. Optical microscopy, electron microscopy and STXM measurements were performed by me. The theoretical predictions presented in the manuscript were developed by Cécile Fradin, Liu Yu and me. I developed the Matlab codes used to analyze optical and electron microscopy data. Optical microscopy results were analyzed by me, electron

microscopy images were analyzed by Murtuza Rajkotwala and me, and STXM measurements were analyzed by Adam Hitchcock and me. I wrote a first complete draft of this manuscript, which has then been revised and modified by Cécile Fradin. The manuscript was still in preparation at the writing of this thesis.

# Misalignment between magnetic moment and cell axis in magnetotactic bacteria *Magnetospirillum magneticum* AMB-1

**Lucas Le Nagard[1], Liu Yu[1], Murtuza Rajkotwala[1], Solomon Barkley[1,2], Dennis A. Bazylinski[3], Adam P. Hitchcock[4] and Cécile Fradin[1]**

[1] Department of Physics and Astronomy, McMaster University, 1280 Main St. W, Hamilton, ON L8S 4M1, Canada

[2] Harvard Paulson School, Harvard University, 29 Oxford Street, Cambridge, MA 02138, USA

[3] School of Life Sciences, University of Nevada, 4505 S. Maryland Pkwy, Las Vegas, NV 89154, USA

[4] Department of Chemistry and Chemical Biology, McMaster University, 1280 Main St. W, Hamilton, ON L8S 4M1, Canada

E-mail: `fradin@physics.mcmaster.ca`

July 2018

**Abstract.** While most quantitative studies of the trajectories of magnetotactic bacteria heavily rely on the premise that the cells' magnetic moment is aligned with their direction of motion, this assumption has never really been challenged. Here we use non-motile cells of *Magnetospirillum magneticum* AMB-1, observed with both electron and phase contrast microscopy, to show that in this species the magnetic moment is in fact not exactly aligned with the axis of the cell body's helix framework. By reconstructing, for each individual cell, the rotation of the cell axis around its magnetic moment, we show that this misalignment is, on average, 6°, and can be as high as 20°. We further propose a method to correct for this misalignment, which leads to a non-biased measurement of the magnetic moment of single cells based on the analysis of their orientation distribution. Using this correction, we measure an average magnetic moment in excellent agreement with the value obtained from the analysis of electron microscopy images. Our findings implies that the motion of magnetic bacteria placed in external magnetic fields might be more complex than usually assumed, and also exhibit some important cell-to-cell individuality.

*Keywords*: Biomagnetism, magnetotaxis, cell structure, magnetosomes, microscopy.

## 1. Introduction

Originally discovered by Bellini [1] in 1963, and later independently re-discovered by Blakemore [2], magnetotactic bacteria (MTB) are Gram-negative prokaryotes ubiqui-

tous in freshwater and marine habitats [3]. They are characterized by their ability to produce magnetosomes, *i.e.* single magnetic domain crystals of either magnetite ($Fe_3O_4$) or greigite ($Fe_3S_4$) surrounded by a lipid membrane [4]. These organelles confer a permanent magnetic moment to MTB, which as a result act as self-propelled micro-compasses swimming along magnetic field lines, presumably in search of favorable growth conditions [5, 6]. Several of the most thoroughly studied MTB species (MS-1 [7], MSR-1 [8], AMB-1 [9]) belong to the *Magnetospirillum* genus. These strains all present a similar helical morphology, with a polar flagellum at each end of the cell [10]. A rigid protein filament, formed by the actin-like protein MamK and extending across the cell, serves as a linear scaffold along which the magnetosomes of magnetotactic spirilla are assembled into a chain [11, 12, 13, 14].

High resolution methods such as transmission electron microscopy (TEM) [15, 16, 17] or electron holography [18, 19] allow for a direct visualization of the magnetosome chain, and have shown that in magnetic spirilla, the magnetosome chain is more or less aligned with the cell body helical axis. By extension, perfect alignment of the cells' magnetic moment with their long axis (when it exists) and with their swimming direction is usually taken for granted in all MTB species. However, when it comes to a precise determination of the orientation of the magnetic moment, the possible deformations induced during TEM sample preparation are a drawback. In addition, TEM does not provide the direction of the magnetization in individual magnetosomes, which makes it difficult to establish the orientation of the magnetic moment for magnetosome chains that are not perfectly linear. Indeed, non-linear geometries of the magnetosome chains are often observed [13, 20, 21].

A precise determination of the alignment between magnetic moment and swimming direction is important when trying to predict MTB's distribution of orientations or trajectories in a magnetic field. In particular, the accuracy of magnetic moment measurements based on cell trajectories or orientation distribution heavily depends on the validity of equating cell direction with magnetic moment direction [22, 23, 24, 25]. Although MTB certainly approximately follow magnetic field lines, their alignment with magnetic field direction is not perfect, and the contribution of thermal noise is often hard to disentangle from other effects, especially for live cells [25, 26]. A misalignment between magnetic moment and swimming direction will cause MTB to rotate around the magnetic field lines in helical trajectories, and will broaden the orientation distribution. Helical trajectories have indeed been observed for a few species, a strong hint that magnetic moment and cell axis might not be exactly aligned, at least for some MTB [27, 28].

In this work, we present calculations predicting how a misalignment between magnetic moment ($\vec{\mu}$) and cell axis ($\vec{L}$) affects the orientation distribution of MTB placed in a uniform external magnetic field. We show that cells with misaligned $\vec{\mu}$ may have a double-peaked orientation distribution as a result of cell body rotation around $\vec{\mu}$. We

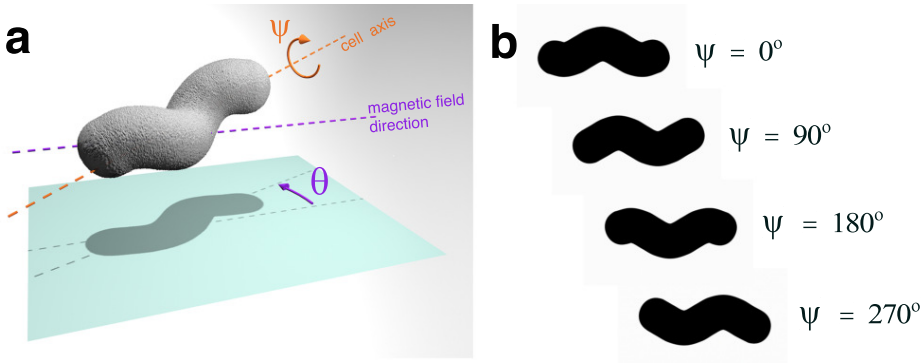


Figure 1: **(a)** Schematic representation of a helical cell, showing the two angles that can be determined by phase microscopy, the apparent cell orientation in the focal plane, $\beta$, and the rotation of the cell body around the helical cell axis, $\alpha$. The purple and orange dashed lines show the direction of the magnetic field, $\vec{B}$, and cell axis, $\vec{L}$, respectively. **(b)** Projection of the cell in the focal plane for different rotations of the cell body around its helical axis.

then use phase microscopy to test this prediction in AMB-1 cells. We take advantage of the helical shape of spirilla, which allows to determine both the projection of $\vec{L}$ in the focal plane and the cell body rotation around $\vec{L}$, and we show that the cell rotation around $\vec{\mu}$ can indeed be detected, proving that $\vec{\mu}$ is not perfectly aligned with $\vec{L}$. For AMB-1, the misalignment is 6° on average and does not depend on cell length ($L$), but is more severe at small $\mu/L$ where it can reach almost 20°. Finally, we demonstrate that taking into account the magnetosome chain misalignment allows using the cell orientation distribution to perform a precise measurement of its magnetic moment.

## 2. Theory: Deviation between cell body axis and magnetic field

In this section, we derive the expected orientation distribution of a magnetotactic bacteria placed in a constant uniform horizontal magnetic field ($\vec{B}$), taking into account a possible misalignment between cell body axis and magnetic moment. When observing spirilla in phase microscopy experiments, two angles related to cell orientation can be determined from the recorded projected shape of the cell in the focal plane (Fig. 1). The first is the apparent orientation of the cell axis with respect to the magnetic field direction, *i.e.* the angle $\theta$ between $\vec{B}$ and the horizontal projection of $\vec{L}$. The second is the angle $\psi$ by which the cell has rotated around its helical axis. We are thus interested in calculating the probability $p(\theta, \psi)$ to find the cell in a certain orientation.

### *2.1. Influence of thermal motions*

We first briefly consider the simple case, treated before in the literature, where the magnetic moment is aligned with the cell axis, and fluctuations in the orientation of

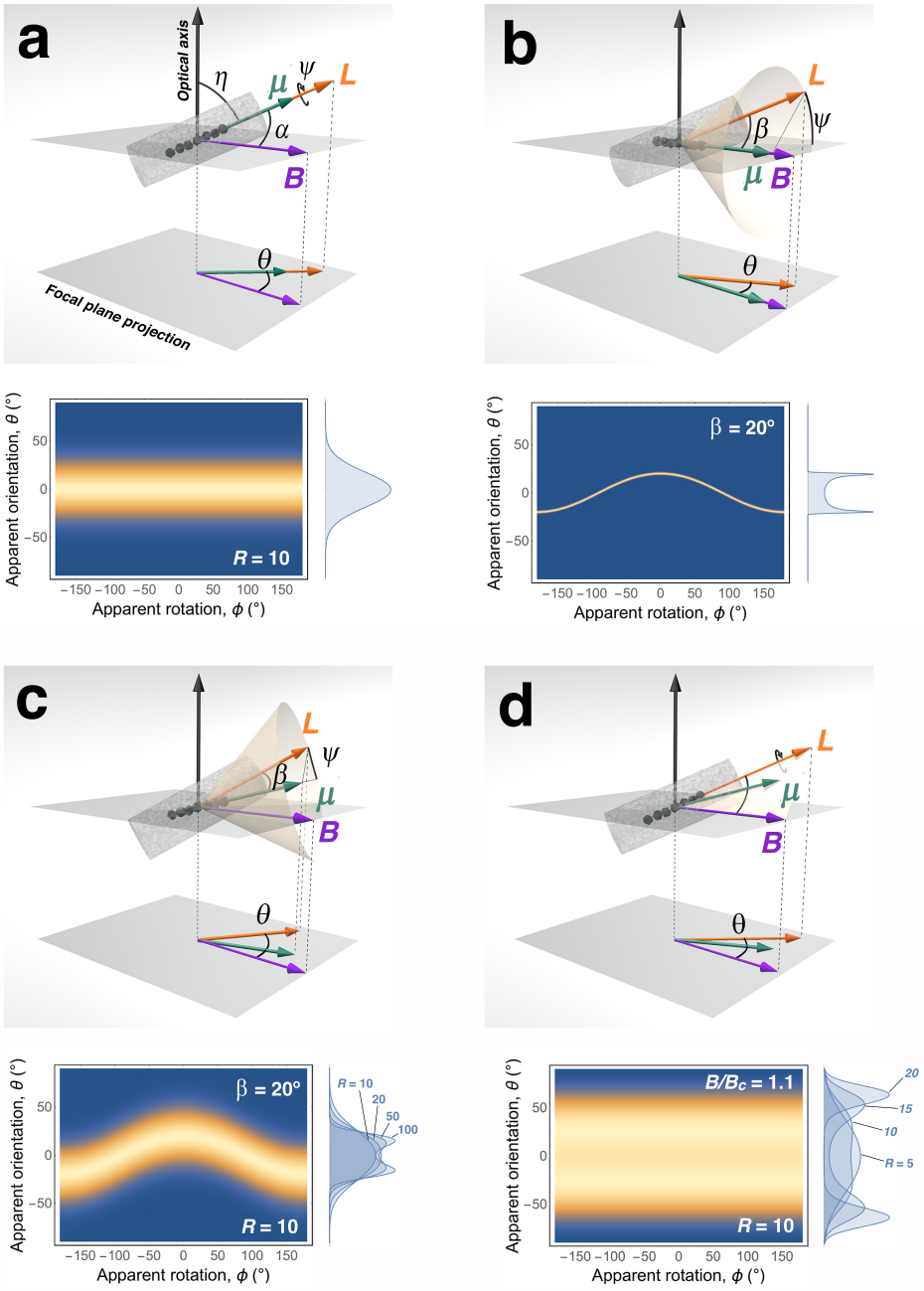


Figure 2: **(a)** Geometry in the absence of misalignment between $\vec{\mu}$ and $\vec{L}$, but considering fluctuations away from $\vec{B}$ due to thermal noise. **(b)** Geometry in the presence of a permanent misalignment between $\vec{\mu}$ and $\vec{L}$ ($\vec{\mu}$ aligned with $\vec{B}$ and $\vec{L}$ rotating on a cone). **(c)** Geometry in the presence of both a permanent misalignment between $\vec{\mu}$ and $\vec{L}$ and thermal fluctuations. **(d)** Geometry in the presence of thermal fluctuations and no permanent misalignment between $\vec{\mu}$ and $\vec{L}$, but instead a varying misalignment due to magnetic susceptibility anisotropy. Note that in this case $\vec{\mu}$ is always found in the plane defined by $\vec{B}$ and $\vec{L}$. For each panel, the expected distribution of orientations is shown at the bottom.

$\vec{\mu}$ are due to thermal noise [15, 29, 3, 25]. The orientation of the cell is characterized

by three angles, defined in Fig. 2a: the azimuthal angle $\theta$ (which is also the apparent orientation of the cell in the focal plane), the inclination with respect to the optical axis, $\eta$, and the rotation around the cell axis, $\psi$. The orientation of the cell is described by Boltzmann statistics, similarly to that of atoms in a paramagnetic material. The probability density associated with a certain orientation depends on the magnetic energy $\vec{\mu}.\vec{B} = \mu B \cos\alpha = \mu B \sin\eta \cos\theta$:

$$p_{T,3D}(\theta, \eta) = \frac{R}{4\pi \sinh(R)} e^{R \sin\eta \cos\theta}, \tag{1}$$

where $T$ is the absolute temperature, and we have defined the ratio $R = \mu B/kT$, which describes the balance between magnetic and thermal energy.

The probability density for $\theta$, the apparent angle between $\vec{B}$ and $\vec{L}$ (as measured by microscopy in the focal plane), can then be calculated exactly by integrating Eq. 1 over all possible inclinations:

$$p_T(\theta) = \frac{R}{4 \sinh(R)} \left[ L_{-1}(R\cos\theta) + I_1(R\cos\theta) \right], \tag{2}$$

where $L_{-1}$ is the modified Struve function of the first kind of order -1 and $I_1$ is the modified Bessel function of order 1. Note that in this simple case, there is no dependence on cell body rotation, $\psi$, as illustrated in the lower panel of Fig. 2a.

For a typical value of the magnetic moment ($\mu \simeq 10^{-16} - 10^{-15}\ A.m^2$) and a sufficiently high magnetic field ($B \simeq 1\ mT$ and above), such that $R \gg 1$, the result is well approximated by the distribution obtained considering that the cell is constrained to a two-dimensional motion in the focal plane [25]:

$$p_T(\theta) \simeq \frac{1}{2\pi I_0(R)} e^{R\cos\theta}, \tag{3}$$

where $I_0$ is the modified Bessel function of order 0.

### *2.2. Influence of a misalignment between cell magnetic moment and cell body*

We next consider another limiting case, where the magnetic moment is perfectly aligned with the magnetic field ($\alpha = 0$, which is expected in the limit where $R \to \infty$), but where there is a misalignment between magnetic moment and cell body axis ($\beta \neq 0$, see Fig. 2b). The cell can then take any orientation on a cone of aperture $2\beta$ aligned with the magnetic field. For a small misalignment ($\beta \ll \pi/2$), the rotation of the cell body around this cone can be equated to the rotation of the cell body around its own axis, $\psi$. The apparent orientation of the cell body is then directly related to $\psi$, with $\theta(\psi) = \tan^{-1}[\tan\beta \cdot \cos\psi]$. In other words:

$$p_M(\theta, \psi) = \frac{1}{2\pi} \delta\left(\theta - \tan^{-1}[\tan\beta \cdot \cos\psi]\right), \tag{4}$$

where $\delta(x)$ represents the Dirac delta function.
As the cell rotates around its magnetic moment ($\psi$ passing from 0 to $2\pi$), the apparent cell orientation varies between $-\beta$ and $\beta$. Assuming a uniform distribution for $\psi$ (as expected if the cell rotates freely around its magnetic moment due to thermal motion), the expected apparent orientation distribution of the cell is non-zero only in the interval $[-\beta, +\beta]$ and can be calculated in this interval by integrating Eq. 4 over $\psi$, yielding:

$$p_M(\theta) = \frac{1}{\pi \cos^2\theta} \frac{1}{\sqrt{\tan^2\beta - \tan^2\theta}}. \tag{5}$$

This apparent orientation distribution has two very sharp peaks, at $-\beta$ and $+\beta$ (lower right panel of Fig. 2b).

### *2.3. Combined effects of thermal motion and misalignment*

In a real system, we expect both a small constant misalignment between magnetic moment and cell body and a small fluctuating misalignment between magnetic moment and magnetic field due to thermal motions (Fig. 2c). As long as these angles remain small ($\beta < 20°$, $R > 5$), we can consider that these two effects just add up, such that the cell apparent orientation probability can be obtained by convolution of the two previously obtained probability distributions:

$$p(\theta, \psi) \simeq \int_{\theta-\beta}^{\theta+\beta} p_T(\chi)\, p_M(\theta - \chi, \psi)\, d\chi, \tag{6}$$

leading to:

$$p(\theta, \psi) \simeq \frac{1}{(2\pi)^2 I_0(R)} e^{R\cos\left[\theta - \tan^{-1}[\tan\beta \cdot \cos\psi]\right]}. \tag{7}$$

The probability distribution $p(\theta, \psi)$ has a very distinctive pattern (shown in the lower panel of Fig. 2c), that combine features from both $p_T(\theta)$ and $p_M(\theta, \psi)$. Most striking is the characteristic sine-like dependence between $\theta$ and $\psi$, a result of the constraint existing between rotation of the cell around its magnetic moment and rotation around its body axis.

Eq. 7 can be integrated numerically over $\psi$ (lower right panel of Fig. 2c) to find the apparent angle distribution $p(\theta)$. This distribution changes from a single central peak at low values of $\beta$ to two symmetric peaks found just below at $-\beta$ and $+\beta$ at higher values of $\beta$. The higher $R$, the sharper the peaks, however the position of the peaks itself remains mostly unchanged as it is set by the value of the misalignment $\beta$.

### *2.4. Misalignment between $\vec{\mu}$ and $\vec{L}$ due to magnetic susceptibility anisotropy*

A second possible scenario leading to a misalignment between cell axis and magnetic moment is the effect of a negative anisotropy in the magnetic susceptibility of the magnetosome chain. Such an anisotropy exists in magnetite, and is also typical of

elongated magnetic materials. It would affect the magnetic potential energy of the magnetosome chain placed in a uniform magnetic field, which would become [30]:

$$E(\alpha) = -\mu B \cos\alpha - \frac{V\Delta\chi B^2 \cos^2\alpha}{2\mu_0}, \tag{8}$$

where $V$ is the volume of the magnetosome chain, $\Delta\chi$ is the anisotropy of magnetic susceptibility and $\mu_0$ is the vacuum permeability. The presence of the quadratic term in Eq. 8 implies that, if $\Delta\chi < 0$ (which is true for magnetite), and for fields larger than the critical value $B_c = -\mu_0\mu/(V\Delta\chi)$, the energy minimum is no longer found at $\alpha = 0$, but instead at $\alpha = \cos^{-1}[B_c/B]$. As a result, we expect a misalignment between $\vec{\mu}$ and $\vec{L}$ for $B > B_c$, increasing as $B$ increases (Fig. 2d). However, contrary to the previous case (constant misalignment due to cell geometry), the direction of $\vec{\mu}$ is not linked to the cell rotation $\psi$, instead $\vec{\mu}$ always lays in the plane defined by $\vec{L}$ and $\vec{B}$.

Taking into account thermal motions leads to the following equation for the orientation distribution in the focal plane (assuming that, as in the simple case considered in section 2.1, it can be assimilated to the distribution that would be obtained if motions were in fact restricted to the focal plane, which is correct for large $R$):

$$P(\theta) = e^{R\left(cos\theta - \frac{1}{2}\frac{B}{B_c}cos^2\theta\right)}/\mathcal{Z}, \tag{9}$$

with the partition function:

$$\mathcal{Z} = \int_{-\pi}^{\pi} e^{R\left(cos\theta - \frac{1}{2}\frac{B}{B_c}cos^2\theta\right)} d\theta. \tag{10}$$

The orientation distribution has two symmetric peaks, whose position varies with the magnitude of the field and whose width varies with $R$ (lower right panel in Fig. 2d). Neither the position nor the width of the peaks depend on $\psi$.

## 3. Methods

### *3.1. AMB-1 cultures*

AMB-1 cells were grown in liquid medium in heterotrophic conditions [31]. The growth medium contained, per liter: 1.0 mL modified Wolfe's mineral elixir [32, 33], 0.1 g $KH_2PO_4$, 0.15 g $MgSO_4{\cdot}7H_2O$, 2.38 g HEPES, 0.34 g $NaNO_3$, 0.1 g yeast extract, 3.0 g BD Bacto Soytone, 4.35 mL potassium lactate (60% solution) and 5 mL Fe (III) citrate 10 mM solution. The pH was adjusted to 7 and dissolved $O_2$ was removed by bubbling $N_2$ in the medium. $O_2$ was added in the culture flasks before inoculation (1.5 % final concentration in the headspace).

### *3.2. Optical microscopy*

*Sample preparation.* MTB were harvested 3 to 6 days after inoculation and immediately killed by heating at 50°C for 15 minutes. The bacterial suspension was then

diluted with fresh medium (1:10 dilution) and injected into custom-made observation chambers. The chambers were made of a glass slide and a coverslip separated by two melted parafilm spacers, creating a channel of approximately 1 cm in length, 5 mm in width and between 100 and 200 $\mu$m in height. The channels were sealed with vacuum grease to avoid evaporation.

*Data collection.* Samples were studied with an upright microscope (Nikon Eclipse E200-LED) using a 40× phase contrast objective. The stage of the microscope was modified to install two custom-made electromagnetic coils (3.6 cm in diameter, 4 cm coil spacing, copper wire, 300 loops per coil) reinforced by two iron cores. Constant magnetic fields parallel to the focal plane were applied by circulating a current through the coils, using an Agilent 33120A power supply connected to an Agilent 33502A amplifier. Movies of dead bacteria in constant fields (1.0 and 1.9 mT) were acquired with a Prosilica GE (Allied Vision) camera at 100 frames per second.

*Data analysis.* A Matlab code was written to determine the cell morphology and orientation from binarized microscopy images. For each frame of the recorded movies, the cell was first translated to the origin and its orientation was approximated by fitting the cell body to a straight line. The cell was then rotated by the corresponding angle to make it approximately horizontal. Pixels were binned vertically to obtain a line corresponding to the cell backbone, which was then fitted by a sine function. These two steps (rotation and fitting) were repeated 16 times for each cell, for rotation angles covering a $\pm 8^\circ$ interval around the angle obtained with the line fit ($1^\circ$ steps). The angle leading to the minimum error in the sine fit was recorded and two additional angles were tested around it, respectively at -0.5° and +0.5°. The angle corresponding to the minimum error after that last step was recorded as the cell orientation, and other parameters of interest (phase $\phi$ and amplitude of the sine function, length of the cell) were also saved. A similar strategy was previously used by Constantino *et al.* to measure the orientation of another helical bacteria, *Helicobacter pylori* [34].

For a cell with helical shape whose direction is not too far from horizontal, the projection of the cell body in the focal plane has a sinusoidal shape. The phase of this sinusoidal shape, $\phi$, is directly related to the rotation of the cell around the helical axis, $\psi$ (as illustrated in Fig. 1). One has: $\psi = \phi + \delta$, where $\delta$ is a geometrical phase shift. In the end, it follows from Eq. 4 that the following relationship should be expected between $\phi$ and $\theta$ (two quantities which are experimentally accessible with phase microscopy):

$$\theta(\phi) = \tan^{-1}\left(\tan\beta \cdot \cos(\phi + \delta)\right). \tag{11}$$

*Orientation distribution analysis* All experimentally measured orientation distributions were plotted as histograms, with a bin width of 2°. They were then compared to the distribution expected in the small angle limit for simple Boltzmann statistics

(Eq. 3), by using discrete Boltzmann statistics, in which case an excellent approximation for Eq. 3 is given by:

$$p(\theta_n) = e^{R\cos\theta_n}/\mathcal{Z}, \text{ with } \mathcal{Z} = \sum_{\theta_i} e^{R\cos\theta_i}. \tag{12}$$

Fit of experimental distributions with Eq. 12 allow extracting a value for $R = \mu B/kT$, from which $\mu$ can be calculated.

### *3.3. Transmission electron microscopy (TEM)*

Samples were prepared by deposition and subsequent drying in air at room temperature of a droplet of growth medium onto a formvar-coated TEM grid. Unstained bacteria were imaged using a JEOL 1200EX TEMSCAN microscope. To estimate the orientation of the magnetic moment of individual cells, the magnetosome chain was divided into short segments. The orientation of each segment was determined through linear least square fitting and the volume of magnetic material in each segment was estimated by assuming a spherical shape for the magnetosomes. The orientation of the total magnetic moment was determined by computing the volume-weighted average orientation of all segments. The orientation of the cell body was measured using the sine fit method described above.

### *3.4. Scanning transmission X-ray microscopy (STXM)*

Samples were prepared exactly as for TEM. STXM measurements were done at the HERMES beamline (SOLEIL synchrotron) using a 40 nm outer zone Fresnel zone plate, by measuring a stack of images at the Fe $L_3$ edge (704-717 eV) with right circularly polarized (RCP) X-rays. Data analysis was performed using aXis2000. X-ray absorption spectra obtained for each magnetosome subchain were compared to reference spectra for magnetite [35]. For a given light polarization, the absorption spectrum depends on the material's direction of magnetization. Comparison to reference spectra is thus used to determine the relative direction of magnetization of each subchain.

## 4. Results

In order to test the hypothesis of a misalignment between $\vec{L}$ and the magnetosome chain in AMB-1, we first imaged 50 cells with electron microscopy and for each of these cells we estimated the direction of the cell axis based on cell shape, and the direction of the magnetic moment based on the morphology of the magnetosome chain (Fig. 3). We found that a misalignment exists for a significant number of cells and measured an average difference of 6.1° between magnetosome chain direction and body axis for the studied population.

An important assumption made when determining the direction of the magnetic moment from TEM images is that all segments in the magnetosome chain have their magnetic

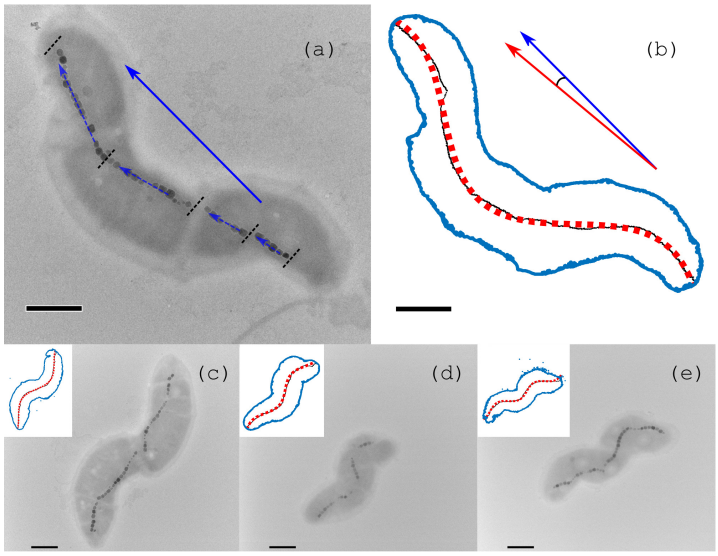


Figure 3: TEM images suggest there is a small structural misalignment between cell body axis and magnetosome chain in AMB-1 cells. **(a)** The magnetic moment orientation of the cell (blue arrow) is determined by adding the contributions of each of the magnetosome subchains (dashed blue arrows). **(b)** The cell axis is determined by approximating the cell backbone to a sine function, as illustrated here for the cell shown in (a). The edges of the cell are shown in blue, the backbone obtained by binning the pixels constituting the cell in black, and the sinusoidal function fitted to the backbone in red. The misalignment between cell axis (red arrow) and chain axis (blue arrow) was 5.2° in this case. **(c, d, e)** Additional examples of AMB-1 cells with different degrees of misalignment (11.2°, 1.2° and 0.6°, respectively). Corresponding sine fit analysis are shown in the insets. Scale bars: 400 nm.

moments pointing in the same overall direction. However, AMB-1 cells often present a magnetosome chain fragmented into subchains separated by gaps. Thus reversals of the magnetic polarity between subchains are possible, as already observed for another magnetic spirillum, MV-1 [36]. We indeed observed this phenomenon in an AMB-1 cell imaged with STXM, using right circularly polarized X-rays (Fig. 4). Magnetosome chains with opposite polarities are clearly visible in the 3-component false-color composite image of that cell shown in Fig. 4a. The difference between the absorption spectra of chains rendered in red and that of those rendered in blue is shown in Fig. 4b. It is in agreement with the reference X-ray magnetic circular dichroism (XMCD) signal of magnetite [35]. This confirms that blue and red subchains have opposite polarities. The possible presence of magnetic reversals, which cannot be detected with standard TEM observation, along with possible alteration of the cell morphology upon drying of the sample, makes TEM not fully reliable for measuring a misalignment between magnetosome chain and cell body.

To more precisely and confidently measure the misalignment between magnetosome chain and cell body axis suggested by TEM images, we studied 111 cells with optical

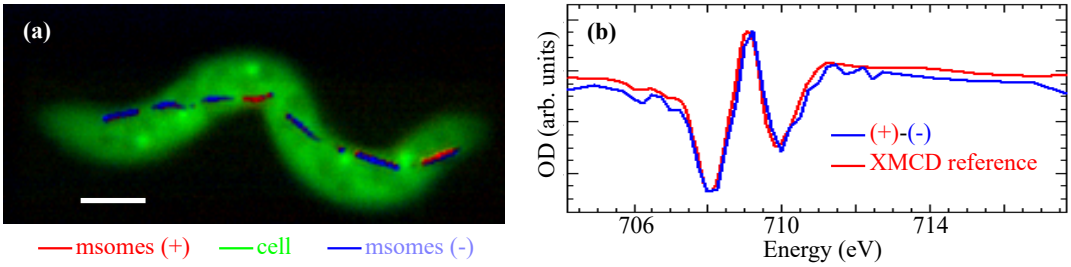


Figure 4: Colorized STXM image of an AMB-1 cell. **(a)** 3-component false color map showing the regions of the sample associated with the three principal absorption spectra observed in this sample: the cell (green), and magnetosome subchains with opposite polarities (blue, red). Scale bar: 500 nm. **(b)** Optical density (OD) signal obtained by subtracting the average blue magnetosomes' signal to the average red magnetosomes' signal, compared to the reference X-ray magnetic circular dichroism (XMCD) signal of magnetite [35].

microscopy in a constant field (B = 1.03 mT). For each cell and for each image of this cell in the recorded movie, the apparent orientation of the cell in the focal plane and its rotation around its body axis were determined, using the sine fit method detailed in the Methods (section 3.2). The orientation distributions of three typical cells are presented in Fig. 5a, d and g. In some cases (a,d), the discrepancy between the orientation distribution and the expected Boltzmann distribution was quite evident, with some cells clearly displaying a two-peaked distribution (a). Such an effect is expected either if the magnetosomes have a strong magnetic susceptibility anisotropy or if there is a permanent misalignment between magnetic moment and cell axis. To distinguish between these two scenarios, the apparent orientation of the cell with respect to the magnetic field direction, $\theta$, was then plotted as a function of its rotation around the cell axis, $\phi$, for each cell. In all cases, the relationship observed between $\theta$ and $\phi$ was consistent with the behaviour predicted by Eq. 7 and 11 (Fig. 5b, e and h). This strongly suggests that the misalignment observed between $\vec{B}$ and $\vec{L}$ is due to a permanent misalignment between magnetosome chain and cell axis, as opposed to susceptibility anisotropy. Using Eq. 11 to fit the experimentally established relationship between $\theta$ and $\phi$ allowed us to very precisely measure the misalignment $\beta$ for each cell.

As seen in section 2.3, the existence of a misalignment of the magnetosome chain broadens the orientation distribution and can lead to two-peaked distributions in extreme cases (as observed for example in Fig. 5a). This in turn affects the value of the magnetic moment extracted from the orientation distribution by fitting it with standard Boltzmann statistics. In the small angle limit, the effects of thermal noise and misalignment add up. Orientation distributions can thus be corrected by subtracting the best fit line obtained with Eq. 11 (red line in Figs. 5b, e, h) to the experimental value of $\theta(\phi)$ (blue symbols in the same figures). The corrected distributions are governed by thermal fluctuations only, and can thus be fitted with Eq. 12 to measure $\mu$ (Fig. 5c, f and i). The values of $\mu$ obtained after data correction are, as expected, generally higher

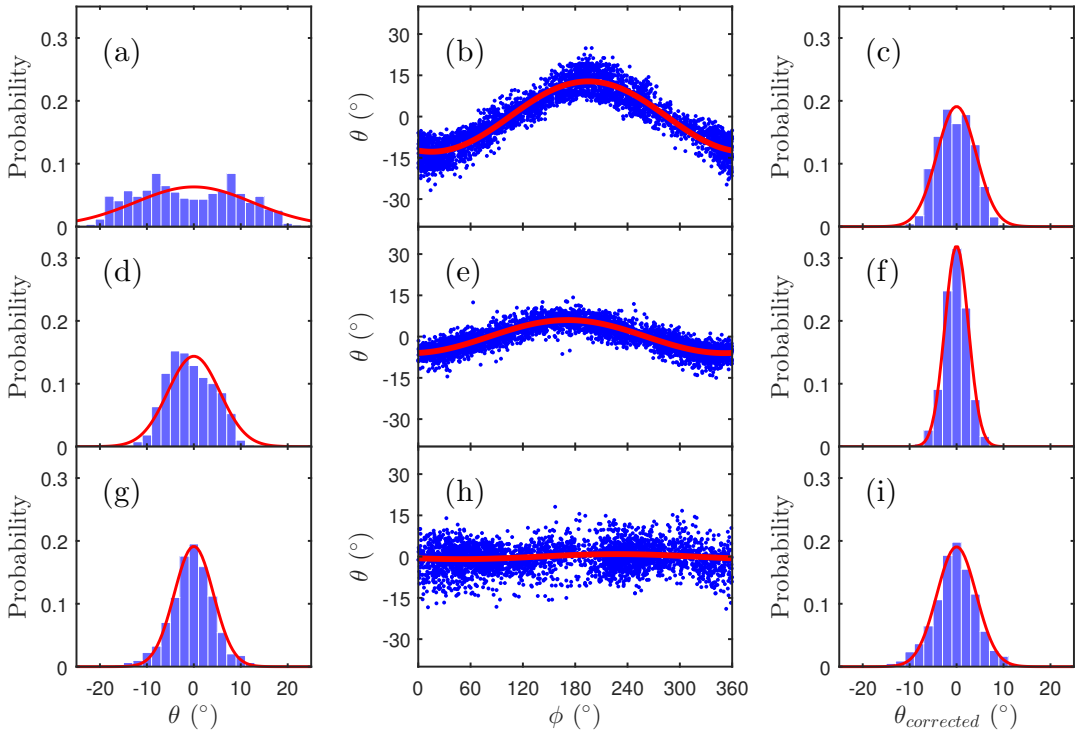


Figure 5: Measurement and correction of the misalignment for three different bacteria in a constant 1.03 mT magnetic field. **(a, d, g)** Experimental orientation distributions. Eq. 12 fitted to these histograms (solid red line) returns magnetic moments $\mu = 0.84 \times 10^{-16}$ A.m$^2$, $\mu = 4.3 \times 10^{-16}$ A.m$^2$ and $\mu = 7.7 \times$ A.m$^2$ respectively for (a), (d) and (g). **(b, e, h)** Relationship between $\theta$ and $\phi$. Eq. 11 fitted to experimental data returns misalignments $\beta = 13°$, $\beta = 6°$ and $\beta = 1°$ respectively for (b), (e) and (h). **(c, f, i)** Corrected orientation distributions obtained after subtraction of the phase-dependent artefact caused by the misalignment. Eq. 12 fitted to these corrected histograms (solid red line) returns magnetic moments $\mu = 7.7 \times 10^{-16}$ A.m$^2$, $\mu = 21 \times 10^{-16}$ A.m$^2$ and $\mu = 7.6 \times 10^{-16}$ A.m$^2$ respectively for (c), (f) and (i).

than before correction, and sometimes very significantly when $\beta$ is large.

In order to verify that the effect of the magnetic susceptibility anisotropy is negligible, we studied a single cell at two different magnetic field strengths (Fig. 6). The same misalignment was measured and similar values of the magnetic moment were obtained after correcting for this misalignment, confirming that the anisotropy of magnetic susceptibility can be neglected for the values of the field tested in this work. In addition, it demonstrates that the contribution of the misalignment to the orientation distributions is effectively corrected by subtracting Eq. 11.

The distribution of misalignments measured by analyzing orientation distributions for AMB-1 cells is peaked between 5° and 7° with an average misalignment of 6.5°. We also observed a positive correlation between the cell length and its magnetic moment

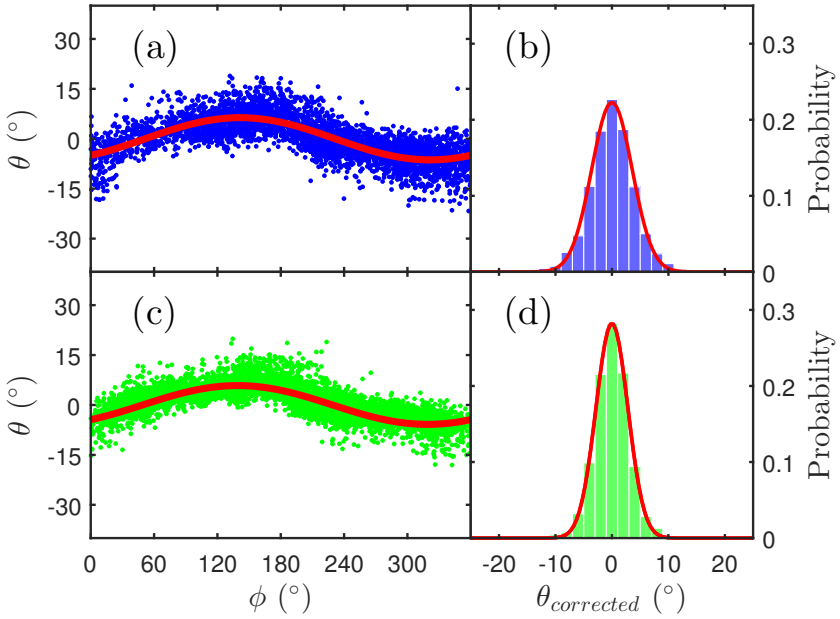


Figure 6: Magnetic moment measurement for the same cell at two different magnetic field strengths. **(a, c)** Relationship between $\theta$ and $\phi$ obtained at 1.03 mT (a) and 1.89 mT (c). Eq. 11 fitted to experimental data returns the same misalignment $\beta = 6°$ in both cases. **(b, d)** Corrected histograms obtained by subtracting Eq. 11 to the data and then subtracting the mean value ($-0.1°$ for (b) and $0.5°$ for (d)) to centre the histograms. Eq. 12 fitted to these corrected histograms (solid red line) returns magnetic moments $\mu = 10 \times 10^{-16}$ A.m$^2$ for (b) and $\mu = 9.0 \times 10^{-16}$ A.m$^2$ for (c).

(Fig. 7(b)) and a negative correlation between the misalignment and the ratio $\mu/L$ (Fig. 7(c)).

## 5. Discussion

The very prescribed relationship we observed, for every single AMB-1 cell we studied, between the apparent cell orientation in the focal plane, $\theta$, and the cell rotation around its axis, $\phi$, exactly follows the form predicted for a cell rotating around an axis slightly different from its cell body axis (Eq. 11). This clearly demonstrates that there is a small permanent misalignment between cell body axis and magnetosome chain for AMB-1 cells, which causes an apparent deviation from an ideal Boltzmann orientation distribution. We also observed that this misalignment is not affected by the strength of the magnetic field. This indicates that the potential effect of the susceptibility anisotropy is negligible for AMB-1 at the considered field strengths and that the only allowed rotation for dead cells is around the magnetic field axis. The magnetic moment of non-motile cells is therefore on average aligned with the field and subject to thermal fluctuations.

We described two methods to measure the misalignment between magnetic moment and cell axis. TEM imaging provides high-resolution images allowing for a direct as-

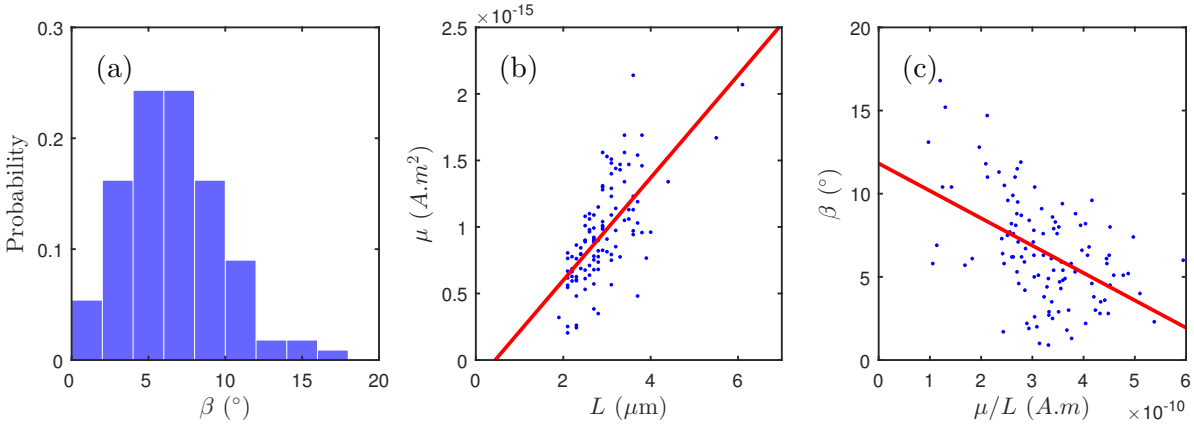


Figure 7: Summary of results for all 111 AMB-1 cells studied. **(a)** Misalignment distribution. The mean value is 6.5° and the standard deviation 3.2°. **(b)** Relationship between $L$ and $\mu$. The Pearson correlation coefficient is $PCC = 0.7$. The red line is a linear fit to the data ($\mu = aL - b$, with $a = 3.8 \times 10^{-10}$ A.m and $b = 1.7 \times 10^{-16}$ A.m$^2$). **(c)** Relationship between $\beta$ and $\mu/L_{cell}$. $PCC = -0.5$ and the red line is a linear fit to the data ($\beta = -a\mu/L + b$, with $a = 1.6 \times 10^{16}$ °.A$^{-1}$.m$^{-1}$ and $b = 12°$).

sessment of the amount of magnetic material in individual cells and an estimate of magnetic moment direction based on the assumption that all magnetosome moments in a subchain are aligned. However, the cell morphology can be altered during sample preparation. Moreover, STXM measurements show that in some cells, not all the subchains that constitute the magnetosome chain possess the same magnetic polarity. We did not investigate the frequency of these magnetic reversals in AMB-1, but this finding is consistent with previous results collected in strain MV-1 [36]. The second method presented here relies on the analysis of movies recorded with phase contrast microscopy. The relative loss of accuracy due to low-resolution imaging is compensated by the acquisition of a large number of frames for each bacteria (minimum 1500 frames per cell), leading to an effective measurement of the misalignment with Eq. 11.

The existence of a misalignment can have multiple origins. First, it seems plausible that the rigid MamK protein filament the magnetosomes attach to in the cytoplasm is not always perfectly aligned with the cell axis. Second, Orue and coworkers showed that the magnetic moment of individual magnetosomes is not aligned with the axis of the magnetosome chain in strain MSR-1 [21]. Instead, the moment of each crystal makes an angle of approximately 20° with the axis of the chain and the chain adopts a helical shape. Since AMB-1 and MSR-1 are morphologically similar, the same behaviour could be expected in AMB-1, which complicates even more the simple assumption of a linear chain aligned with the cell axis.

Surprisingly, this work is to our knowledge the first to report and measure the misalignment between cell axis and magnetic moment in magnetospirilla. This might be

explained by the fact that most studies that involve tracking MTB in a field are performed on live bacteria. The fast rotation of the cell complicates the detection of the misalignment. Yet, this phenomenon is significant since the distribution of misalignments recorded has a mean of 6.5°, with a significant number of cells having a misalignment higher than 10°. The method presented here provides a way to correct the misalignment in order to recover non-biased orientation distributions for the cell magnetic axis, from which the magnetic moment of individual MTB can be measured. Fig. 6 presents data measured at two different field strengths on the same cell. A significant difference is observed between the magnetic moments measured for that specific cell respectively before correction ($\mu = 3.5 \times 10^{-16}$ and $\mu = 2.9 \times 10^{-16} A.m^2$ at respectively 1.03 and 1.89 mT) and after correction ($\mu = 10 \times 10^{-16}$ and $\mu = 9.0 \times 10^{-16} A.m^2$ at respectively 1.03 and 1.89 mT). This demonstrates that a 6° misalignment is sufficient to significantly alter the measurement of $\mu$ made from the analysis of the orientation distribution.

As seen in Fig. 7 (b), $\mu$ increases with L. This could be explained by the fact that longer cells can accommodate longer magnetosome chains within their cytoplasm. This correlation is interesting, because it means that long cells do not limit their magnetosome production to the strict minimum required to align them in an external magnetic field. In addition, a negative correlation between $\beta$ and $\mu$/L is obtained. This relationship can be explained by the fact that for a given L, higher values of $\mu$ mean longer and/or more linear magnetosome chains, thus limiting the magnitude of a possible misalignment.

It is interesting to compare the values of the average magnetic moment obtained from corrected orientation distributions on the one hand, and TEM on the other hand. Corrected orientation distributions returned an average magnetic moment $\mu_{av} = 10 \times 10^{-16} A.m^2$ with standard deviation $\sigma = 4 \times 10^{-16} A.m^2$. We also estimated the average saturation magnetic moment with TEM [25, 37], by multiplying the average volume of magnetite per cell by the saturation magnetization of magnetite ($M_{sat} = 4.8 \times 10^{-22} A.m^2.nm^{-3}$ [38]). We studied 50 cells and found this value to be $\mu_{sat} = 12 \times 10^{-16} A.m^2$ with standard deviation $\sigma = 4 \times 10^{-16} A.m^2$. This value is larger than the one we previously reported using the same method [25], probably due to several improvements made in the bacterial culture methods. The average length of the population studied with TEM is smaller than the one studied with optical microscopy (2.2 $\mu$m vs 2.9 $\mu$m respectively). Using the linear relationship between $\mu$ and $L$ obtained in Fig. 7a, a corrected value of the average magnetic moment assuming an average length of 2.2 $\mu$m is obtained: $\mu_{2.2} = 6.5 \times 10^{-16}$ A.m$^2$. As expected, this value is lower than the saturation magnetization, since only a weak magnetic field is applied. Moreover, our TEM estimation of $\mu_{sat}$ does not take into account the fact that the subchains are not perfectly aligned, and that in some cases they have opposite polarities.

Our results significantly differ from values reported for AMB-1 in other studies ($\mu =$

$1.0 \times 10^{-16} A.m^2$ from iron uptake [39], $\mu = 0.5 \times 10^{-16} A.m^2$ from optical magnetic imaging [40], $\mu = 0.7 \times 10^{-16} A.m^2$ from vibrating sample magnetometry [41], $\mu = 0.9 - 7.1 \times 10^{-16} A.m^2$ from a variety of other techniques [25]). These differences can be explained by differences in culturing, but also by the fact that since our method is based on single-cell measurements, only cells that exhibit a magnetic response are studied. After correction of the misalignment, the orientation distribution method used here provides non-biased values of the magnetic moment. Our method is based on a direct fitting of the corrected orientation distributions, with only two external parameters: the magnetic field strength and the absolute temperature, two easily measurable quantities.

Although the average misalignment is small, it has a significant impact on the orientation distributions of dead cells and on the magnetic moment measurement, as seen for the cell presented in Fig. 6. More importantly, this misalignment is likely to affect the swimming motion of individual cells. To swim, MTB rotate their flagella, which in turn forces the cell body to rotate. A natural assumption to make is that the rotation axis corresponds to the cell axis. But if a misalignment exists, the rotation around the cell axis creates a misalignment between the magnetic moment and the field, which is unfavorable at high fields. Since each cell is characterized by a specific magnetic moment and a specific misalignment, this needs to be studied at the single cell level.

## References


[1] Bellini S 2009 *Chinese Journal of Oceanology and Limnology* **27** 3–5
[2] Blakemore R 1975 *Science* **190** 377–379
[3] Blakemore R P 1982 *Annual Reviews in Microbiology* **36** 217–238
[4] Uebe R and Schüler D 2016 *Nature Reviews Microbiology* **14** 621
[5] Frankel R B, Bazylinski D A, Johnson M S and Taylor B L 1997 *Biophysical journal* **73** 994–1000
[6] Lefèvre C T, Bennet M, Landau L, Vach P, Pignol D, Bazylinski D A, Frankel R B, Klumpp S and Faivre D 2014 *Biophysical journal* **107** 527–538
[7] Maratea D and Blakemore R 1981 *International Journal of Systematic and Evolutionary Microbiology* **31** 452–455
[8] Schleifer K H, Schüler D, Spring S, Weizenegger M, Amann R, Ludwig W and Köhler M 1991 *Systematic and Applied Microbiology* **14** 379–385
[9] Matsunaga T, Sakaguchi T and Tadakoro F 1991 *Applied Microbiology and Biotechnology* **35** 651–655
[10] Balkwill D, Maratea D and Blakemore R 1980 *Journal of Bacteriology* **141** 1399–1408
[11] Arakaki A, Webb J and Matsunaga T 2002 *Journal of Biological Chemistry*
[12] Komeili A, Li Z, Newman D K and Jensen G J 2006 *Science* **311** 242–245
[13] Scheffel A, Gruska M, Faivre D, Linaroudis A, Plitzko J M and Schüler D 2006 *Nature* **440** 110
[14] Draper O, Byrne M E, Li Z, Keyhani S, Barrozo J C, Jensen G and Komeili A 2011 *Molecular microbiology* **82** 342–354
[15] Frankel R B and Blakemore R 1980 *Journal of Magnetism and Magnetic Materials* **15** 1562
[16] Bazylinski D A, Garratt-Reed A J and Frankel R B 1994 *Microscopy research and technique* **27** 389–401
[17] Lefèvre C T and Bazylinski D A 2013 *Microbiology and Molecular Biology Reviews* **77** 497–526

[18] Dunin-Borkowski R E, McCartney M R, Frankel R B, Bazylinski D A, Pósfai M and Buseck P R 1998 *Science* **282** 1868–1870
[19] Dunin-Borkowski R E, McCartney M R, Pósfai M, Frankel R B, Bazylinski D A and Buseck P R 2001 *European Journal of Mineralogy* **13** 671–684
[20] Faivre D and Schuler D 2008 *Chemical Reviews* **108** 4875–4898
[21] Orue I, Marcano L, Bender P, García-Prieto A, Valencia S, Mawass M, Gil-Cartón D, Venero D A, Honecker D, García-Arribas A *et al.* 2018 *Nanoscale* **10** 7407–7419
[22] ESQUIVEL D M S and DE BARROS H G L 1986 *Journal of experimental biology* **121** 153–163
[23] Ērglis K, Wen Q, Ose V, Zeltins A, Sharipo A, Janmey P A and Cēbers A 2007 *Biophysical journal* **93** 1402–1412
[24] Penninga I, de Waard H, Moskowitz B M, Bazylinski D A and Frankel R B 1995 *Journal of Magnetism and Magnetic Materials* **149** 279–286
[25] Nadkarni R, Barkley S and Fradin C 2013 *PloS one* **8** e82064
[26] Zhu X, Ge X, Li N, Wu L F, Luo C, Ouyang Q, Tu Y and Chen G 2014 *Integrative Biology* **6** 706–713
[27] Pan Y, Lin W, Li J, Wu W, Tian L, Deng C, Liu Q, Zhu R, Winklhofer M and Petersen N 2009 *Biophysical journal* **97** 986–991
[28] Yang C, Chen C, Ma Q, Wu L and Song T 2012 *Journal of Bionic Engineering* **9** 200–210
[29] Kalmijn A 1981 *IEEE Transactions on Magnetics* **17** 1113–1124
[30] Lemaire B, Davidson P, Ferré J, Jamet J, Panine P, Dozov I and Jolivet J 2002 *Physical review letters* **88** 125507
[31] Le Nagard L, Morillo-López V, Fradin C and DA B 2018 *Journal of Visual Experiments* **in production**
[32] Wolin E, Wolin M and Wolfe R 1963 *Journal of Biological Chemistry* **238** 2882–2886
[33] Bazylinski D A, Dean A J, Schüler D, Phillips E J and Lovley D R 2000 *Environmental microbiology* **2** 266–273
[34] Constantino M A, Jabbarzadeh M, Fu H C and Bansil R 2016 *Science advances* **2** e1601661
[35] Goering E, Lafkioti M, Gold S and Schuetz G 2007 *Journal of Magnetism and Magnetic Materials* **310** e249–e251
[36] Kalirai S S, Bazylinski D A and Hitchcock A P 2013 *PLoS One* **8** e53368
[37] Zahn C, Keller S, Toro-Nahuelpan M, Dorscht P, Gross W, Laumann M, Gekle S, Zimmermann W, Schüler D and Kress H 2017 *Scientific Reports* **7** 3558
[38] Haynes W M 2014 *CRC handbook of chemistry and physics* (CRC press)
[39] Smith M, Sheehan P, Perry L, OConnor K, Csonka L, Applegate B and Whitman L 2006 *Biophysical journal* **91** 1098–1107
[40] Le Sage D, Arai K, Glenn D, DeVience S, Pham L, Rahn-Lee L, Lukin M, Yacoby A, Komeili A and Walsworth R 2013 *Nature* **496** 486
[41] Krichevsky A, Smith M, Whitman L, Johnson M, Clinton T, Perry L, Applegate B, OConnor K and Csonka L 2007 *Journal of applied physics* **101** 014701

## 3.3 Magnetosome biomineralization and magnetism studied with STXM

This section presents the main results of STXM experiments performed to study the biomineralization process. In order to study the chemical composition of growing magnetosome crystals in a time-course manner (*i.e.* at different stages of the biomineralization process), a culture was first made non-magnetic by removing the principal sources of iron from the growth medium. This iron-starved culture was then transferred into fresh, iron-rich medium to induce biomineralization. Samples were prepared at different stages of the biomineralization process and measured at the synchrotron facilities. The first section of this chapter presents results of STXM measurements performed on cells grown only in iron-rich medium. These measurements provide a reference signal that correspond to the signal obtained at the end of the time-course, when magnetosomes are made of pure magnetite. The second section presents the main results of the time-course experiments. It includes a conference paper that summarizes the main findings, and supplementary results that provide more details about the results obtained on the time-course sample prepared 8 hours after inducing biomineralization. Time-course measurements are challenging, as they require a high spatial resolution and long acquisition times to increase the signal-to-noise ratio. An evolution of the magnetosome signal is observed during the time-course, which indicates that STXM is a suitable tool to study biomineralization.

### 3.3.1 XAS and XMCD of cells grown in iron-rich conditions

In the AMB-1 species, the magnetosome chain is often divided into short subchains, each of them possessing a permanent moment. The XAS of each subchain thus depends on the orientation of its magnetic moment with respect to the polarization of the X-ray beam (LCP or RCP). The reference spectra used for magnetite in this study were recorded by Goering [49], with RCP and LCP. Interestingly, some AMB-1 cells possess magnetosome subchains that do not all have their magnetic moment pointing in the same direction (Fig. 3.2). This surprising result was obtained by comparing the spectra of different subchains in a single cell imaged with only one polarization (RCP), and observing that some subchains match the Goering-LCP reference while

some others match the Goering-RCP spectrum. In both cases, the experimental spectra are in good agreement with the reference, which confirms that AMB-1 produces relatively high purity crystals.

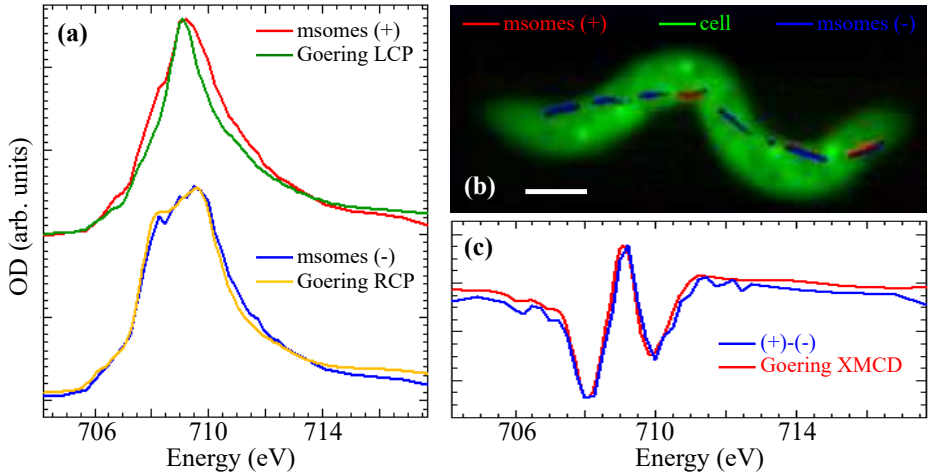


Figure 3.2: One-polarization (RCP) stack on an AMB-1 cell grown in iron-rich medium. **(a)** Spectra obtained for the different magnetosome subchains inside the cell (blue and red), compared to Goering's reference spectra (green and yellow). **(b)** 3-component false color composite obtained by fitting the stack with three spectra: the two magnetosome signals, and a spectrum extracted from the cell. Blue and red magnetosomes have opposite polarity. **(c)** Goering's XMCD reference spectrum (blue) and experimental XMCD signal (blue) obtained by taking the difference of both magnetosome signals. Experiment performed at the Soleil-HERMES beamline.

The presence of subchains with opposite polarities reduces the total magnetic moment of the cell and can contribute to the existence of a misalignment between the moment and the cell axis. Opposite polarities inside a single cell have been observed before in a significant number of MTB belonging to the MV-1 species [51], and the results presented in Fig. 3.2 show that this can also happen in AMB-1. One should note that the analysis performed here is not a real XMCD measurement, since only one polarization has been used. However, the signal presented in Fig. 3.2 (c) is in very good agreement with the reference. This is because two magnetosome polarities are present in this cell, and this shows that for the spectroscopy, changing the polarization from RCP to LCP is equivalent to flipping the polarity of the studied magnetic material. An XMCD map, *i.e.* the difference of two images recorded wit LCP and

RCP at a single energy corresponding to a peak in the XMCD spectrum, recorded on the same cell confirmed the relative orientations of the subchains in that cell.

### 3.3.2 Time-course results

This section presents the results of the time-course experiments. It starts with a conference paper that will be presented at the International Conference on X-ray Microscopy (XRM 2018, Saskatoon, Canada) and that is published in *Proceedings of Microscopy & Microanalysis 2018*. This paper details the questions we want to address and summarizes the main findings. It was written by Adam Hitchcock based on experiments performed by Xiaohui Zhu and myself. The second part of this section focuses on the sample prepared eight hours after inducing biomineralization.

# How do Magnetotactic Bacteria Synthesize Magnetite ? – a Soft X-ray Spectroscopy, Spectromicroscopy and Magnetism Time Course Study

Lucas Le Nagard,[1] Xiaohui Zhu,[2] Adam P. Hitchcock,[1,2] Dennis A. Bazylinski,[3] Sufal Swaraj,[4] Stephan Stanescu[4] and Rachid Belkhou[4]

[1.] Department of Physics, McMaster University, Hamilton, Canada
[2.] Department of Chemistry & Chemical Biology, McMaster University, Hamilton, Canada
[4.] School of Life Sciences, University of Nevada-Las Vegas, Las Vegas, USA
[4.] Synchrotron Soleil, St. Aubin, France
* Corresponding author, aph@mcmaster.ca

Prokaryote and archaeon magnetotactic bacteria (MTB) biomineralize chains of single-domain, $Fe_3O_4$ nanoparticles, known as magnetosomes. Magnetosomes, which are arranged in chains inside the cell, function as a strong magnetic dipole so the cell aligns with the earth's magnetic field. Coupled with oxygen sensing (aerotaxis), magneto-aerotaxis is believed to increase the efficiency of the MTB in finding their optimal $O_2$ concentration in the sediments (the interface of oxic and anoxic zones) [1]. As one of the simplest biomineralizing microorganisms, MTB are an ideal model to study biomineralization mechanisms. Although the genetic control is actively under study and a conserved core of genes has been identified, the chemical steps in magnetosome biomineralization are still not fully understood. Several competing hypotheses exist. Frankel *et al.* [2] reported that $(Fe^{3+})_2O_3 \cdot 0.5H_2O$, an amorphous ferrihydrite, precursor, is formed first, which is then partially reduced and dehydrated to $Fe_3O_4$. However, Faivre *et al.* [3] did not observe any mineral precursor in a time-resolved Mössbauer study and suggested that Fe(II) and Fe(III) quickly co-precipitate to directly form $Fe_3O_4$ within magnetosome vesicles. In a recent study [4], we observed hematite ($\alpha$-$Fe_2O_3$) in MV-1 MTB, which was likely a precursor in magnetosome $Fe_3O_4$ formation. We are investigating biomineralization in AMB-1 MTB cells using Fe L-edge X-ray absorption spectra (XAS) and X-ray magnetic circular dichroism (XMCD) of individual cells and magnetosomes measured by Scanning Transmission X-ray Microscopy (STXM). The measurements are made at the Hermes STXM at Soleil, as well as at CLS aSTXM. We use a time-course approach. We start with non-magnetic cells (grown in absence of Fe); initiate magnetosome formation by adding Fe to the culture; and sample at various stages of magnetosome growth and chain formation. Once dried on a TEM grid the cells are dead and stable. By measuring the Fe chemistry inside representative cells, and the magnetism of nascent magnetosomes, we probe how MTB synthesize $Fe_3O_4$ magnetosomes. A combined TEM, XAS study of AMB-1 time course samples was reported earlier [5], but they only measured average Fe L-spectra of many cells, not inside individual cells.

We sampled the time course at 0 min (just before adding the Fe-depleted cells to Fe-containing media), 10 min, 30 min, 1 hr, 2 hr, 4 hr, 8 hr and 48 hr. Fe $L_{2,3}$-edge XAS measurements were performed on these AMB-1 samples. Transmission electron microscopy of the time course samples at McMaster showed that magnetosomes appeared in some cells after 4-8 hours. Fe $L_3$ STXM-XAS results (single spectra at 709.2 eV, the $L_3$ peak; Fe maps from 2 images ($OD_{709}$-$OD_{704}$); or full spectra fit) at Soleil showed that near complete magnetosomes were present at 4 hr, although many of them were very small and had a different spectrum from magnetite. Only a few immature, isolated magnetosomes were observed in the 1 or 2 hr samples. By 48 hr, the cells examined were indistinguishable from normally cultured AMB-1 cells, both in terms of imaging (**Fig. 1**), and Fe $L_3$ spectra (**Fig. 2**). The 8 hr sample showed immature magnetosomes in a disorganized pattern as well as short chains of normal magnetite. A weak cytoplasmic signal, with clear Fe(III) character, was observed in the 2 hr and 4 hr samples.

A challenge of our first set of measurements was the presence of culture salts in the samples. Since then we have greatly improved sample preparation by careful washing, and by fixation**,** as indicated in Fig. 3. Although results to date deal mostly with method development and anecdotal evidence, it is already clear that the time-course method applied to individual AMB-1 cells will be an effective tool to systematically probe how magnetotactic bacteria take up Fe ions from the local environment, and transform them into $Fe_3O_4$ magnetosomes. Results are expected to address the following questions. *Are there precursor cytoplasmic solution or solid species formed before mature magnetosome formation? If so, what is the chemical state of these precursors? How, and at what rate, are these precursors converted into mature magnetite magnetosomes ?* [6]

References:


[1] D. Faivre and D. Schuler, Chem.Rev.**108** (2008) 4875.
[2] R. B. Frankel, et al., Biochim. Biophys. Acta **763** (1983) 147.
[3] D. Faivre, et al., Angew. Chem., Int. Ed. Engl **46** (2007) 8495
[4] X.H. Zhu, et al. , Proc. Nat. Acad. Sci **113** (2016) E8219.
[5] S. Stanisland, et al., Proc. Nat. Acad. Sci. **104** (2007) 19524.


[6] CLS is supported by CFI. We thank Soleil for beamtime.


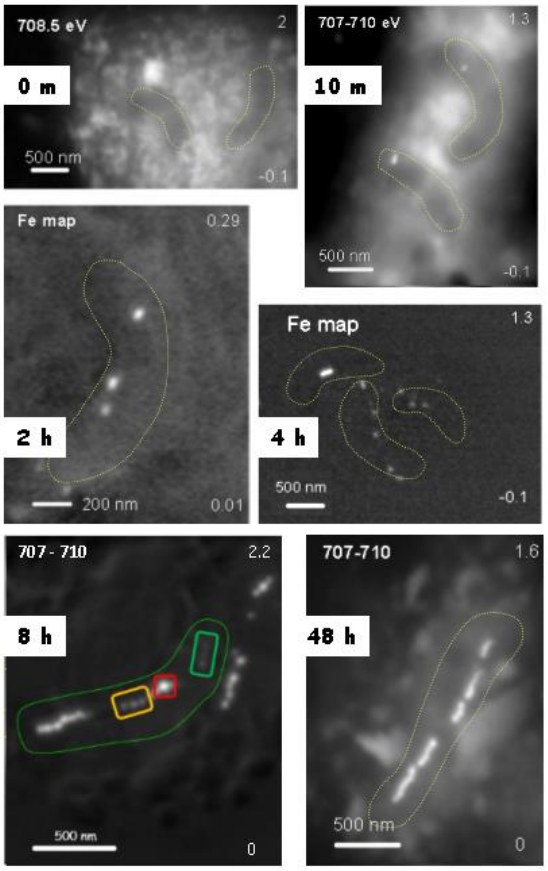


**Fig. 1.** Single or multi energy images (0, 10 m; 8 hr, 48 hr) or Fe maps from fits (2 hr, 4 hr) of time course AMB-1 cells derived from STXM Fe $L_3$ stacks, Cell outlines derived from TEM images of same area. 3 colored areas in 1 cell of the 8 hr sample have different Fe $L_3$ spectra. (Soleil)

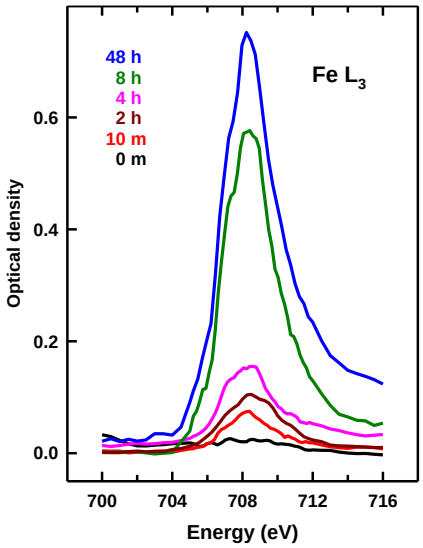


**Fig. 2.** Fe $L_3$ spectra of magnetosomes or precursors (Soleil).

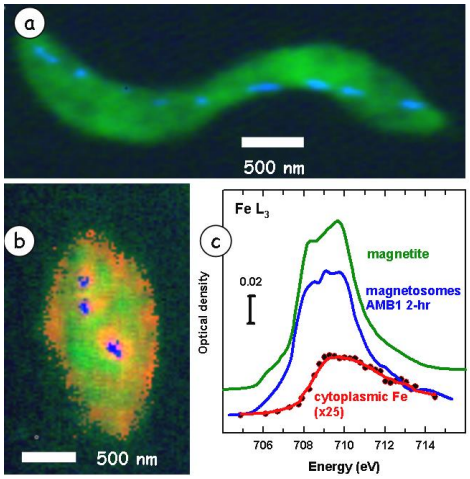


**Fig. 3.** Fe $L_3$ analysis of improved AMB-1 cell preparation (no extra-cellular materials). (a) gluteraldehyde fixed 48-hr time course (green – cell, blue – mature magnetosomes) . (b) phosphate buffer wash, 2-hr time course (green - cell, red-cyto-Fe, blue – early magnetosomes). (c) Comparison of Fe $L_3$ spectra of pure magnetite (blue), magnetosomes in 2-hr sample (green), and cytoplasmic Fe (red). (CLS)

### Supplementary results: 8-hour time-course sample

The 8-hour time-course sample is interesting because it displays magnetosomes at different stages of the biomineralization process (Fig. 3.3). In the middle of the cell, one or two large magnetosomes exhibit a spectrum very similar to the one of mature magnetite (Fig. 3.3 (b)&(c), red). Close to these mature crystals, a few magnetosomes display a similar spectrum, but with a less pronounced shoulder around 708 eV (Fig. 3.3 (b)&(c), orange). Finally, a weak signal that is in good agreement with the reference spectrum for Fe (III) is obtained in the upper part of the cell (Fig. 3.3 (b)&(c), green). This signal is attributed to magnetosome precursors, and it thus seems that biomineralization in AMB-1 starts with precursors principally made of Fe (III). This finding is consistent with observations made by Zhu and coworkers [60] with ptychography. Staniland and coworkers also observed an Fe(III) signal in the early stages of the biomineralization process, and attributed this signal to hematite ($Fe_2O_3$) [61]. Part of the iron must then be reduced during crystal growth in order to form magnetite.

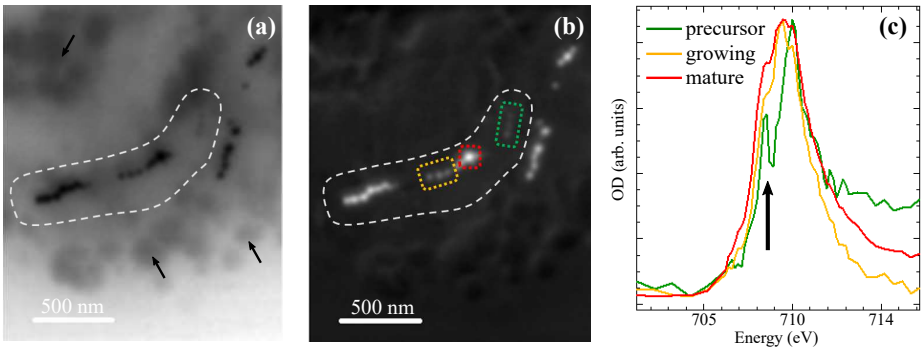


Figure 3.3: 8-hour time-course sample. **(a)** Transmission image recorded at 709.2 eV. The dash line shows the shape of the studied cell. Dark particles are magnetosomes. Black arrows indicate salt or organic compounds coming from the growth medium. **(b)** Iron OD map obtained by subracting the 700 eV OD image to the 709.2 eV OD image. Orange, red and green rectangles indicate magnetosomes at different stages of the biomineralization process. **(c)** Absorption spectra corresponding to the three regions selected in (b). The black arrow indicates the spectral region that changes the most between different growth stages. Experiment performed at the Soleil-HERMES beamline.

It can be seen in Fig. 3.3 that salts and organic compounds present in the medium significantly decrease the image quality, making it difficult to distinguish the cell. The white dash line drawn in Fig. 3.3 (b)&(c) is based on a TEM image recorded on the same region to identify the shape of the cell. Sample preparation protocols involving the fixation of the cells with glutaraldehyde are promising, since the cells can then be redispersed in deionized water, eliminating artefacts coming from the presence of salts and organic matter. Significant image quality improvement was observed when using this technique to study a 48-hour time-course sample (XRM 2018 paper, Fig. 3 (a)). The magnetosomes are not affected by this new protocol, however it is not known yet if the iron signal coming from the cytoplasm is modified or not.

# Chapter 4

# Conclusion

Magnetotactic bacteria have developed an impressive strategy to optimize their motion in search of favorable growth conditions. Mostly microaerophilic, MTB require a specific amount of $O_2$ to survive and develop normally. In nature (*i.e.* in lakes, ponds or sediments), the amount of dissolved $O_2$ generally decreases from the surface towards deeper regions. The most efficient way to locate favorable conditions is thus to navigate principally in the vertical direction and to stay at a stable depth once a suitable $O_2$ concentration is found. Magneto-aerotaxis enables MTB to do just that, using the inclined geomgnetic field lines as a preferred direction of motion. This is made possible by the intracellular chain of magnetosomes that confer to each cell a permanent magnetic moment, causing it to align with external magnetic fields.

In the work presented in this thesis, we used an interdisciplinary approach to address two main questions: Is the magnetic moment aligned with the cell axis ? What are the intermediate iron species involved in the biomineralization process ? In a first project, we developed a theory that predicts the effect of a misalignment between magnetic moment and cell axis, and performed experiments on dead bacteria that show that such a misalignment does exist in many cells, with significant consequences on the orientation distributions of individual bacteria. Our method enables us to perform non-biased measurements of the magnetic moment of individual MTB from their orientation distribution, by taking into account this misalignment. In a second project, we used STXM to study the biomineralization process in a time-course

experiment. A method was developed to grow AMB-1 cells with reduced magnetism and to prepare samples suitable for X-ray observation. Preliminary results show that a ferric (Fe(III)) iron oxide is produced first during magnetosome synthesis, before being converted to magnetite. This work thus shows that STXM is a suitable tool to perform these measurements. One obstacle faced during this MSc is the difficulty of the sample preparation itself, since perfectly clean samples are required to study the weak signals expected during magnetosome synthesis.

Understanding how magnetosomes are produced by MTB is interesting from a fundamental point of view, but could also lead to applications that take advantage of the great purity and controlled crystallography of magnetosomes. Investigating the effect of the misalignment on the swimming motion of MTB is also needed to understand if this misalignment gives any advantage to the bacteria or if it is just an illustration of the fact that some variability always exists in biological processes.

# Bibliography


[1] Salvatore Bellini. On a unique behavior of freshwater bacteria. *Chinese Journal of Oceanology and Limnology*, 27(1):3–5, 2009.

[2] Richard B Frankel. The discovery of magnetotactic/magnetosensitive bacteria. *Chinese Journal of Oceanology and Limnology*, 27(1):1–2, 2009.

[3] Richard Blakemore. Magnetotactic bacteria. *Science*, 190(4212):377–379, 1975.

[4] Richard P Blakemore. Magnetotactic bacteria. *Annual Reviews in Microbiology*, 36(1):217–238, 1982.

[5] RP Blakemore, D Maratea, and RS Wolfe. Isolation and pure culture of a freshwater magnetic spirillum in chemically defined medium. *Journal of Bacteriology*, 140(2):720–729, 1979.

[6] Richard B Frankel, Richard P Blakemore, and Ralph S Wolfe. Magnetite in freshwater magnetotactic bacteria. *Science*, 203(4387):1355–1356, 1979.

[7] Christopher T Lefèvre and Dennis A Bazylinski. Ecology, diversity, and evolution of magnetotactic bacteria. *Microbiology and Molecular Biology Reviews*, 77(3):497–526, 2013.

[8] Dennis A Bazylinski, Christopher T Lefèvre, and Dirk Schüler. Magnetotactic bacteria. In *The Prokaryotes*, pages 453–494. Springer, 2013.

[9] Christopher T Lefevre, Fernanda Abreu, Marian L Schmidt, Ulysses Lins, Richard B Frankel, Brian P Hedlund, and Dennis A Bazylinski. Moderately

thermophilic magnetotactic bacteria from hot springs in nevada. *Applied and environmental microbiology*, 76(11):3740–3743, 2010.

[10] Christopher T Lefèvre, Richard B Frankel, Mihály Pósfai, Tanya Prozorov, and Dennis A Bazylinski. Isolation of obligately alkaliphilic magnetotactic bacteria from extremely alkaline environments. *Environmental microbiology*, 13(8):2342–2350, 2011.

[11] Damien Faivre and Dirk Schuler. Magnetotactic bacteria and magnetosomes. *Chemical Reviews*, 108(11):4875–4898, 2008.

[12] Viviana Morillo, Fernanda Abreu, Ana Carolina Araujo, Luiz Gonzaga Paula de Almeida, Alex Enrich Prast, Marcos Farina, Ana Tereza Ribeiro de Vasconcelos, Dennis A Bazylinski, and Ulysses Lins. Isolation, cultivation and genomic analysis of magnetosome biomineralization genes of a new genus of south-seeking magnetotactic cocci within the alphaproteobacteria. *Frontiers in microbiology*, 5:72, 2014.

[13] Tadashi Matsunaga, Toshifumi Sakaguchi, and Fumihiko Tadakoro. Magnetite formation by a magnetic bacterium capable of growing aerobically. *Applied Microbiology and Biotechnology*, 35(5):651–655, 1991.

[14] Karl Heinz Schleifer, Dirk Schüler, Stefan Spring, M Weizenegger, R Amann, Wolfgang Ludwig, and Manfred Köhler. The genus magnetospirillum gen. nov. description of magnetospirillum gryphiswaldense sp. nov. and transfer of aquaspirillum magnetotacticum to magnetospirillum magnetotacticum comb. nov. *Systematic and Applied Microbiology*, 14(4):379–385, 1991.

[15] Toshifumi Sakaguchi, J Grant Burgess, and Tadashi Matsunaga. Magnetite formation by a sulphate-reducing bacterium. *Nature*, 365(6441):47, 1993.

[16] Dennis A Bazylinski, Timothy J Williams, Christopher T Lefevre, Ryan J Berg, Chuanlun L Zhang, Samuel S Bowser, Annette J Dean, and Terrence J Beveridge. Magnetococcus marinus gen. nov., sp. nov., a marine, magnetotactic bacterium that represents a novel lineage (magnetococcaceae fam. nov., mag-

netococcales ord. nov.) at the base of the alphaproteobacteria. *International journal of systematic and evolutionary microbiology*, 63(3):801–808, 2013.

[17] Karen Tavares Silva, Fernanda Abreu, Fernando P Almeida, Carolina Neumann Keim, Marcos Farina, and Ulysses Lins. Flagellar apparatus of south-seeking many-celled magnetotactic prokaryotes. *Microscopy research and technique*, 70(1):10–17, 2007.

[18] Dennis A Bazylinski, Timothy J Williams, Christopher T Lefevre, Denis Trubitsyn, Jiasong Fang, Terrence J Beveridge, Bruce M Moskowitz, Bruce Ward, Sabrina Schübbe, Bradley L Dubbels, et al. Magnetovibrio blakemorei gen. nov., sp. nov., a magnetotactic bacterium (alphaproteobacteria: Rhodospirillaceae) isolated from a salt marsh. *International journal of systematic and evolutionary microbiology*, 63(5):1824–1833, 2013.

[19] Dennis A Bazylinski, Richard B Frankel, Brigid R Heywood, Stephen Mann, John W King, Percy L Donaghay, and Alfred K Hanson. Controlled biomineralization of magnetite (fe (inf3) o (inf4)) and greigite (fe (inf3) s (inf4)) in a magnetotactic bacterium. *Applied and environmental microbiology*, 61(9):3232–3239, 1995.

[20] Mathieu Bennet, Luca Bertinetti, Robert K Neely, Andreas Schertel, André Körnig, Cristina Flors, Frank D Müller, Dirk Schüler, Stefan Klumpp, and Damien Faivre. Biologically controlled synthesis and assembly of magnetite nanoparticles. *Faraday discussions*, 181:71–83, 2015.

[21] René Uebe and Dirk Schüler. Magnetosome biogenesis in magnetotactic bacteria. *Nature Reviews Microbiology*, 14(10):621, 2016.

[22] Arash Komeili, Zhuo Li, Dianne K Newman, and Grant J Jensen. Magnetosomes are cell membrane invaginations organized by the actin-like protein mamk. *Science*, 311(5758):242–245, 2006.

[23] André Scheffel, Manuela Gruska, Damien Faivre, Alexandros Linaroudis, Jürgen M Plitzko, and Dirk Schüler. An acidic protein aligns magnetosomes

along a filamentous structure in magnetotactic bacteria. *Nature*, 440(7080):110, 2006.

[24] Richard B Frankel and Dennis A Bazylinski. Magnetosomes and magneto-aerotaxis. In *Bacterial sensing and signaling*, volume 16, pages 182–193. Karger Publishers, 2009.

[25] Lijun Chen, DA Bazylinski, and BH Lower. Bacteria that synthesize nano-sized compasses to navigate using earths geomagnetic field. *Nature Education Knowledge*, 3(10):30, 2010.

[26] Richard B Frankel, Dennis A Bazylinski, Mark S Johnson, and Barry L Taylor. Magneto-aerotaxis in marine coccoid bacteria. *Biophysical journal*, 73(2):994–1000, 1997.

[27] Lei Yan, Shuang Zhang, Peng Chen, Hetao Liu, Huanhuan Yin, and Hongyu Li. Magnetotactic bacteria, magnetosomes and their application. *Microbiological research*, 167(9):507–519, 2012.

[28] Sylvain Martel, Charles C Tremblay, Serge Ngakeng, and Guillaume Langlois. Controlled manipulation and actuation of micro-objects with magnetotactic bacteria. *Applied Physics Letters*, 89(23):233904, 2006.

[29] Noriyuki Nakamura, J Grant Burgess, Kaoru Yagiuda, Satoko Kudo, Toshifumi Sakaguchi, and Tadashi Matsunaga. Detection and removal of escherichia coli using fluorescein isothiocyanate conjugated monoclonal antibody immobilized on bacterial magnetic particles. *Analytical chemistry*, 65(15):2036–2039, 1993.

[30] Tadashi Matsunaga, Yoshiko Okamura, Yorikane Fukuda, Aris Tri Wahyudi, Yaeko Murase, and Haruko Takeyama. Complete genome sequence of the facultative anaerobic magnetotactic bacterium magnetospirillum sp. strain amb-1. *DNA research*, 12(3):157–166, 2005.

[31] Shimyoung Seong and Tai Hyun Park. Swimming characteristics of magnetic bacterium, magnetospirillum sp. amb-1, and implications as toxicity measurement. *Biotechnology and bioengineering*, 76(1):11–16, 2001.

[32] Rohan Nadkarni, Solomon Barkley, and Cécile Fradin. A comparison of methods to measure the magnetic moment of magnetotactic bacteria through analysis of their trajectories in external magnetic fields. *PloS one*, 8(12):e82064, 2013.

[33] Jinhua Li, Yongxin Pan, Guanjun Chen, Qingsong Liu, Lanxiang Tian, and Wei Lin. Magnetite magnetosome and fragmental chain formation of magnetospirillum magneticum amb-1: transmission electron microscopy and magnetic observations. *Geophysical Journal International*, 177(1):33–42, 2009.

[34] Chen-Dong Yang, Haruko Takeyama, Tsuyoshi Tanaka, and Tadashi Matsunaga. Effects of growth medium composition, iron sources and atmospheric oxygen concentrations on production of luciferase-bacterial magnetic particle complex by a recombinant magnetospirillum magneticum amb-1. *Enzyme and Microbial Technology*, 29(1):13–19, 2001.

[35] U Heyen and D Schüler. Growth and magnetosome formation by microaerophilic magnetospirillum strains in an oxygen-controlled fermentor. *Applied microbiology and biotechnology*, 61(5-6):536–544, 2003.

[36] Edward M Purcell. Life at low reynolds number. *American journal of physics*, 45(1):3–11, 1977.

[37] Eric Lauga and Thomas R Powers. The hydrodynamics of swimming microorganisms. *Reports on Progress in Physics*, 72(9):096601, 2009.

[38] IS Jacobs and CP Bean. An approach to elongated fine-particle magnets. *Physical Review*, 100(4):1060, 1955.

[39] Richard B Frankel and RP Blakemore. Navigational compass in magnetic bacteria. *Journal of Magnetism and Magnetic Materials*, 15(3):1562, 1980.

[40] Richard B Frankel. Magnetic guidance of organisms. *Annual review of biophysics and bioengineering*, 13(1):85–103, 1984.

[41] Charles Rosenblatt, F Flavio Torres de Araujo, and Richard B Frankel. Birefringence determination of magnetic moments of magnetotactic bacteria. *Biophysical journal*, 40(1):83–85, 1982.

[42] Xuejun Zhu, Xin Ge, Ning Li, Long-Fei Wu, Chunxiong Luo, Qi Ouyang, Yuhai Tu, and Guanjun Chen. Angle sensing in magnetotaxis of magnetospirillum magneticum amb-1. *Integrative Biology*, 6(7):706–713, 2014.

[43] Darci Motta S Esquivel and Henrique GP Lins De Barros. Motion of magnetotactic microorganisms. *Journal of experimental biology*, 121(1):153–163, 1986.

[44] J Anthony Seibert and John M Boone. X-ray imaging physics for nuclear medicine technologists. part 2: X-ray interactions and image formation. *Journal of nuclear medicine technology*, 33(1):3–18, 2005.

[45] David Attwood. Soft x-rays and extreme ultraviolet radiation, 1999.

[46] James H Scofield. X-ray data booklet. *X-ray data booklet*, 2001.

[47] Chunmei Chen, James J Dynes, Jian Wang, Chithra Karunakaran, and Donald L Sparks. Soft x-ray spectromicroscopy study of mineral-organic matter associations in pasture soil clay fractions. *Environmental science & technology*, 48(12):6678–6686, 2014.

[48] Joachim Stöhr and Hans Christoph Siegmann. *Magnetism: from fundamentals to nanoscale dynamics*, volume 152. Springer Science & Business Media, 2007.

[49] EJ Goering, M Lafkioti, S Gold, and G Schuetz. Absorption spectroscopy and xmcd at the verwey transition of fe3o4. *Journal of Magnetism and Magnetic Materials*, 310(2):e249–e251, 2007.

[50] Richard AD Pattrick, Gerrit Van Der Laan, C Michael B Henderson, Pieter Kuiper, Esther Dudzik, and David J Vaughan. Cation site occupancy in spinel ferrites studied by x-ray magnetic circular dichroism: developing a method for mineralogists. *European Journal of Mineralogy*, 14(6):1095–1102, 2002.

[51] Samanbir S Kalirai, Dennis A Bazylinski, and Adam P Hitchcock. Anomalous magnetic orientations of magnetosome chains in a magnetotactic bacterium: Magnetovibrio blakemorei strain mv-1. *PLoS One*, 8(1):e53368, 2013.

[52] Harald Ade and Adam P Hitchcock. Nexafs microscopy and resonant scattering: Composition and orientation probed in real and reciprocal space. *Polymer*, 49(3):643–675, 2008.

[53] Weilun Chao, Peter Fischer, T Tyliszczak, Senajith Rekawa, Erik Anderson, and Patrick Naulleau. Real space soft x-ray imaging at 10 nm spatial resolution. *Optics express*, 20(9):9777–9783, 2012.

[54] Lucas Le Nagard, Viviana Morillo-López, Cécile Fradin, and Dennis A Bazylinski. Growing magnetotactic bacteria of the genus magnetospirillum: Strains msr-1, amb-1 and ms-1. *Journal of visualized experiments: JoVE*, 2018 (In Press).

[55] EA Wolin, M_J Wolin, and RS Wolfe. Formation of methane by bacterial extracts. *Journal of Biological Chemistry*, 238(8):2882–2886, 1963.

[56] Dennis A Bazylinski, Annette J Dean, Dirk Schüler, Elizabeth JP Phillips, and Derek R Lovley. N2-dependent growth and nitrogenase activity in the metal-metabolizing bacteria, geobacter and magnetospirillum species. *Environmental microbiology*, 2(3):266–273, 2000.

[57] RS Wolfe, RK Thauer, and N Pfennig. A capillary racetrack method for isolation of magnetotactic bacteria. *FEMS Microbiology Ecology*, 3(1):31–35, 1987.

[58] William M Haynes. *CRC handbook of chemistry and physics*. CRC press, 2014.

[59] Samanbir S Kalirai, Karen P Lam, Dennis A Bazylinski, Ulysses Lins, and Adam P Hitchcock. Examining the chemistry and magnetism of magnetotactic bacterium candidatus magnetovibrio blakemorei strain mv-1 using scanning transmission x-ray microscopy. *Chemical Geology*, 300:14–23, 2012.

[60] Xiaohui Zhu, Adam P Hitchcock, Dennis A Bazylinski, Peter Denes, John Joseph, Ulysses Lins, Stefano Marchesini, Hung-Wei Shiu, Tolek Tyliszczak, and David A Shapiro. Measuring spectroscopy and magnetism of extracted and intracellular magnetosomes using soft x-ray ptychography. *Proceedings of the National Academy of Sciences*, 113(51):E8219–E8227, 2016.

[61] Sarah Staniland, Bruce Ward, Andrew Harrison, Gerrit van der Laan, and Neil Telling. Rapid magnetosome formation shown by real-time x-ray magnetic circular dichroism. *Proceedings of the National Academy of Sciences*, 104(49):19524–19528, 2007.